

UCLA

UCLA Previously Published Works

Title

Dynamic Viscosity and Transverse Ultrasonic Attenuation of Engineering Materials

Permalink

<https://escholarship.org/uc/item/57q7h5xq>

Journal

Applied Sciences, 10(15)

ISSN

2076-3417

Author

Ono, Kanji

Publication Date

2020


DOI

10.3390/app10155265

Peer reviewed

Review

Dynamic Viscosity and Transverse Ultrasonic Attenuation of Engineering Materials

Kanji Ono 

Department of Materials Science and Engineering, University of California, Los Angeles (UCLA), Los Angeles, CA 90095, USA; ono@ucla.edu; Tel.: +1-310-825-5534

Received: 20 July 2020; Accepted: 28 July 2020; Published: 30 July 2020



Abstract: In this paper, ultrasonic attenuation of the transverse waves of engineering materials is evaluated, covering metals, ceramics, polymers, fiber-reinforced plastics, and rocks. After verifying experimental methods, 273 measurements are conducted and their results are tabulated. Fifty of the tests are for the longitudinal mode. Attenuation behavior is determined over broadband spectra. The attenuation spectra are characterized in four patterns, with 2/3 of the tests showing linear frequency dependence and another $\frac{1}{4}$ linear spectrum plus Rayleigh scattering (Mason-McSkimin relation). The longitudinal and transverse damping factors varied from 0.004 to 0.065, which are 1/3 to 5 times those of polymethyl methacrylate, suggesting that almost all the engineering materials tested may be viscoelastic. The present test results make the term *dynamic viscosity* more appropriate for exploring the underlying processes. The observed results were compared between the longitudinal and transverse modes and among similar material types. In more than a half of the tests, the transverse attenuation coefficients were higher than the corresponding longitudinal attenuation coefficients by 1.5× or more. Some material groups had similar attenuation coefficients for the two modes. Since the physical basis for viscous damping is hardly understood, especially in hard solids, further studies from new angles are keenly desired. This collection of new attenuation data will be of value for such works. Practically, this will assist in materials selection and in designing structural health monitoring and non-destructive inspection protocols.

Keywords: dynamic viscosity; ultrasonic attenuation; transverse waves; shear waves; damping factor; metals; ceramics; polymers; fiber-reinforced plastics; rocks; dislocation damping; Mason-McSkimin relation; Rayleigh scattering

1. Introduction

Dynamic viscosity and attenuation of elastic waves have been studied for a long time in geophysics, ultrasonics, and polymer physics [1–4]. The frequency range of interest is below 10 Hz in seismology, above 20 kHz in ultrasonics, and from 20 mHz to 20 MHz in polymer physics. Dynamic mechanical analysis methods determine the storage (or elastic), loss (or viscous), and complex (E^*) moduli, as a function of frequency, temperature, or time [5]. These are especially useful for polymers and fiber reinforced plastics. Geophysicists have used attenuation behavior as a tool to examine the interior of the earth and recently produced Q tomographs, globally mapping the areas of high attenuation [6]. Here, Q is a measure of attenuation and is called the quality factor with $Q^{-1} = \Delta E/2\pi E_m$, where ΔE is energy loss and E_m is the maximum energy stored per cycle [1]. In ultrasonics, damping factor η ($=Q^{-1}$) and attenuation coefficient α ($=\pi\eta/\lambda$ with wavelength λ) are more commonly used. Knopoff [1] showed that η is also related to the viscosity (η_{KV}) term in the Kelvin-Voigt model of viscoelastic solids as $\eta = 2\pi f \eta_{KV}/E'$, with frequency f and the elastic modulus E' . Thus, ultrasonic attenuation induced by damping can be attributed to dynamic viscosity.

Ultrasonic waves are widely used as non-destructive evaluation (NDE) methods to achieve the quality assurance and failure prevention in many industries [3,7,8]. One approach is ultrasonic testing (UT) that uses active interrogation of target components and the other is acoustic emission (AE) that relies primarily on “acoustic” signals emitted from the target under stress. Both are major contributors to the field of structural health monitoring (SHM) [9,10]. In UT and AE applications, attenuation parameters have more passive roles than in seismology, that is, high attenuation often produces poor signal-to-noise ratio when one seeks a high spatial resolution by using higher frequency testing. This requires the knowledge of ultrasonic attenuation coefficients in designing an optimal test strategy. In many SHM applications, guided ultrasonic waves are useful and their attenuation coefficients are related to those of longitudinal and transverse (or shear) waves [11]. However, past studies on experimental determination of attenuation coefficients were limited, especially for transverse wave attenuation [12]. The dearth of transverse wave attenuation is likely due to the lack of practical applications requiring direct transverse wave measurements in UT or AE NDE fields [7,8]. In geophysics, various wave modes are often studied together and the attenuation coefficients for both the longitudinal and transverse modes can be found for rocks in the literature (wave modes being referred to as P and S for compressional and shear). This reflects the importance of seismic S waves since these produce the strongest shaking of the buildings and structures. With the dynamic mechanical analysis for polymers and FRP, the axial and torsional moduli correspond to longitudinal and transverse modes.

For the longitudinal wave attenuation in the MHz range, a recent work measured and provided the attenuation coefficients from 348 tests [13]. The present work is to follow this previous study by first establishing a reliable method for getting transverse wave attenuation coefficients and to fill the extant gap by obtaining them for representative engineering materials. While the transvers \times mode testing was not conducted for all the samples used in [13], more than 270 test results will be presented below. Of the total, 50 tests were for additional longitudinal attenuation testing. The attenuation coefficients for longitudinal and transverse waves can be compared directly as identical samples were used for both tests. For 61% of the tests, the comparison yielded the expected trend of higher transverse wave attenuation, but some materials and material groups exhibited lower (17% of total) or comparable (23%) transverse wave attenuation. The existence of the three trends for seismic wave attenuation was shown analytically in [14]. While the transverse wave attenuation is higher in some rocks, the opposite cases were also reported [1,14,15]. The observed attenuation behaviors reported below are discussed in terms of various damping and scattering mechanisms. As was the case in [13], the current understanding of attenuation mechanisms is found inadequate to explain many of the findings.

In describing the attenuation behavior of materials, additional terms have to be defined. First, the attenuation coefficient is written for the longitudinal and transverse waves as α and α_t . These are frequency dependent, and are usually separable between the linear term and power-law terms. The linear parts, often called damping term, of α and α_t , are written as $C_d f$ and $C_{dt} f$, with frequency f , while the power-law terms as $C_n f^n$ and $C_{nt} f^n$. When damping factors are independent of f , C_d and C_{dt} are unchanged with frequency and we have:

$$\alpha = C_d f \quad (1)$$

and

$$\alpha_t = C_{dt} f \quad (2)$$

where C_d (or C_{dt}) is equal to $\pi v \eta$ (or $\pi v_t \eta_t$) with v (or v_t) being the longitudinal (or transverse) wave velocity and η (or η_t) the longitudinal (or transverse) damping factor.

For many materials in the usual ultrasonic frequency range of 20 kHz to 20 MHz, the linear relations are adequate. Of the power-law relations, $n = 4$ is the most often observed. This arises from

Rayleigh scattering and $C_4 = C_R$ was used in [13]. The corresponding term for the transverse mode is C_{Rt} . A combination of the linear and Rayleigh terms becomes the following for the two wave modes:

$$\alpha = C_d f + C_R f^4 \quad (3)$$

$$\alpha_t = C_{dt} f + C_{Rt} f^4 \quad (4)$$

Equation (3) was called the Mason-McSkimin relation after its first use by Mason and McSkimin [16]. Here, the same name is also used for Equation (4). Additionally, frequency-squared (f^2) and frequency-cubed (f^3) dependences of α were observed in [13] and were named as Datta-Kinra and Biwa relations, respectively [17,18].

In the following, the experimental methods used are described along with the background information in Section 2. Section 3 presents test results of ferrous metals including cast iron, non-ferrous metals, polymers, fiber-reinforced plastics, and ceramics and rocks in five subsections. These are accompanied by discussions for various sub-groups, including comparisons between the longitudinal and transverse attenuation characteristics. Section 4 provides a discussion of the attenuation behavior encompassing different types of materials, followed by the summary and conclusions sections. An Appendix A gives the elastic moduli data of the materials tested in the present study.

2. Experimental Methods

The experimental approach used for transverse wave attenuation is identical to that employed in [13] for longitudinal wave attenuation except for the use of transverse wave transducers. It utilizes through transmission setups as shown in Figure 1, using damped, wideband transducers as both transmitter and receiver. Setup 1 is used for direct contact of the transmitter and receiver, giving the voltage output V_1 from the receiver as a result of transmitter excitation by a pulser. This is also called $\text{fac} \times \text{to-face}$ testing. Setup 2 places sample 1 between the transmitter and receiver, while Setup 3 places sample 2 between the transmitter and receiver. These yield V_2 and V_3 , respectively, in response to pulser excitation. By applying a fast Fourier transform (FFT) on V_1 , V_2 , and V_3 , one gets the corresponding frequency domain spectra R_1 , R_2 , and R_3 , expressed in dB (in reference to 0 dB at 1 V). Expressing the transmitter output (in reference to 0 dB at 1 nm) and receiver sensitivity (in reference to 0 dB at 1 V/nm) as T and R (also in dB), one obtains:

$$R_1 = T + R \quad (5)$$

$$R_2 = T - \alpha_t X_1 - D_1 - T_c + R \quad (6)$$

$$R_3 = T - \alpha_t X_2 - D_2 - T_c + R \quad (7)$$

where X_1 and X_2 are the thickness of sample 1 and 2, D_1 and D_2 are the diffraction correction of sample 1 and 2 given by Equation (8) below and T_c is the transmission coefficient of the sample going from the transmitter to the receiver (Equation (9)), respectively. The diffraction loss D for sample thickness x using two circular transducers of active radius, a , is given by:

$$D = \{[\cos(2\pi/s) - J_1(2\pi/s)]^2 + [\sin(2\pi/s) - J_1(2\pi/s)]^2\}^{0.5} \quad (8)$$

where $s = X v_t / f a^2$, with v_t being the transverse wave velocity. This is due to Rogers and van Buren [19], who integrated the Lommel integral for a circular piston motion, received over the same sized area, located at distance X away. In the UT field, Equation (8) has mostly been applied for the cases of longitudinal waves, but Mielenz [20] showed that it is also applicable to transverse waves since the original Fresnel formulation was for light diffraction. T_c arises from the differences in acoustic impedances of the transducer face (Z_t) and sample (Z_s) and is given by:

$$T_c = (4Z_t Z_s) / (Z_t + Z_s)^2 \quad (9)$$

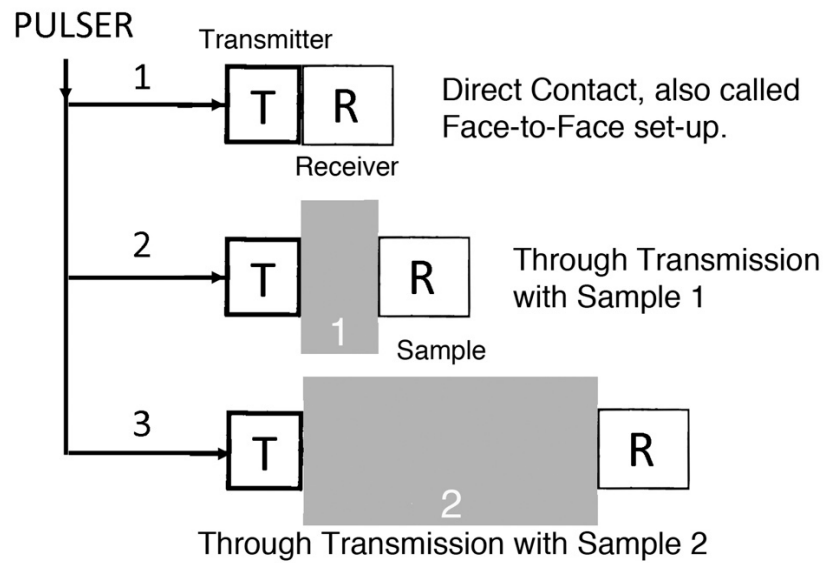


Figure 1. Schematics of attenuation experiment, including 1. direct contact test, 2. and 3. through-transmission test 1 and 2.

In the present setup, transducers (Olympus V221, 10 MHz, 6.4-mm diameter, Olympus NDT, Waltham, MA, USA) have an integral buffer made of fused quartz with $Z_t = 12.91$ Mrays. $|T_c|$ values ranged from 0.01 dB for BK7 glass to 9.07 dB for ultra-high molecular weight polyethylene (UHMWPE).

By using two of three Equations (3a–c), one gets three expressions for the transverse wave attenuation coefficient, α_t :

$$\alpha_t = (R_2 + D_1 - R_3 - D_2)/(X_2 - X_1) \tag{10}$$

$$\alpha_t = (R_1 - R_2 - D_1 - T_c)/X_1 \tag{11}$$

$$\alpha_t = (R_1 - R_3 - D_2 - T_c)/X_2 \tag{12}$$

Equation (10) leads to the first method, called transmission difference method 1 (TDM-1), using Setups 2 and 3. This approach cancels out the effects of transmission coefficient due to acoustic impedance mismatch and the coupling layer effects also cancel. Another is called transmission difference method 2 (TDM-2) using either Equations (11) or (12). That is, TDM-2 uses one sample of thickness X with Setups 1 and 2 (or 3). This is more convenient than TDM-1 because only one sample is needed, but it requires the T_c term and a coupling layer enters into the obtained α_t value. For many of the sample materials in the present study, only one thickness was available and TDM-2 had to be used.

A predecessor of TDMs has been commonly used in geophysics [14,15,21–23]. An aluminum reference block of the same size as rock specimens was typically used and assumed to have zero attenuation. In this direct substitution method, the T_c terms can be small for aluminum and for many rocks and cancel out. The effect of diffraction loss, which was usually not corrected, can be larger; e.g., for $X = 100$ mm, average diffraction losses between aluminum and granite are 1.7 and 1.0 dB for the longitudinal and transverse wave attenuation (over 0.03 to 2 MHz), respectively. Thus, the correction for the diffraction loss is needed for attaining accurate measurements. In addition, the attenuation coefficients of aluminum alloys are small, but not negligible.

In the earliest method for transverse wave attenuation measurements, Mason and McSkimin used quartz disk transducers in 1947 [16]. This method takes advantage of very low loss occurring in the quartz disks, although the reflection loss of 0.4 to 0.7 dB from the disk-mounted surfaces cannot be ignored. Mounting of these delicate disks is difficult and coupling repeatability was challenging, especially for the transmission arrangements. In this study, this method was used on a limited number of samples to verify the level of attenuation obtained by TDM-1 and -2.

The next approach, now called a double through-transmission method, was introduced by Kono [24] in 1960, as a rotating plate method. It is a transmission method through a tilted plate sample for the velocity and attenuation measurements. This has been improved upon both from the uses of advanced analytical tools and of high-precision immersion or air-coupled test systems [25–35]. This was used for fiber-reinforced plastics with much success for the determination of anisotropic elastic moduli. When it is used for attenuation measurements, results were sometimes vastly different from the well-established results of other methods. For example, Wu [30] obtained the attenuation coefficients for longitudinal and transverse waves to be 1050 and 7500 dB/m at 2.2 MHz for polymethyl methacrylate (PMMA). The slope of the same data showed C_d and C_{dt} of 478 and 1740 dB/m/MHz, respectively. The C_d value was much higher than the other reported values on PMMA of $C_d = 85.3$ dB/m/MHz averaged from ten studies [12,13]. Other works [31–34] that relied on the double through-transmission method also reported higher attenuation values as reviewed in [12]. Thus, the double through-transmission method was suspected to suffer from the presence of unrecognized issues, such as the off-normal incidence and refraction of circular wave front [12]. However, Tran et al. [35] using the same method provided significantly lower attenuation results. For PMMA, they obtained $C_d = 101.4$ dB/m/MHz and $C_{dt} = 268$ dB/m/MHz, averaging their 5 and 10 MHz attenuation values. These are comparable to other reported values, confirming the soundness of the double through-transmission method itself. For the transverse attenuation, Hartmann and Jarzynski [36] obtained $C_{dt} = 218$ dB/m/MHz and recent interferometric measurements on PMMA gave $C_{dt} = 253$ dB/m/MHz (average of three slopes) [37]. These three works will be used as reference.

Before embarking on a broad survey of the transverse attenuation coefficients of engineering materials of wide interest, a series of tests were conducted using PMMA as the reference material. This is to confirm that the present test methods provide results consistent with previous studies in the literature. A similar series was also performed for the case of longitudinal wave attenuation [13]. For these tests using TDM-1 and TDM-2, PMMA plates of eight different thicknesses were used, ranging from 5.25 to 27.3 mm. Following transmission tests of PMMA samples of various thicknesses and FFT processing, spectral differences were calculated to produced plots of transverse attenuation versus frequency. Four examples are shown in Figure 2. These include three transverse attenuation spectra of TDM-1 tests, giving the low (blue curve) and high (red) limits and the middle C_{dt} value (green). The red curve shows the worst linear fit ($R^2 = 0.989$). C_{dt} values were obtained from the least square \times fit with the average $R^2 = 0.993$. One TDM-2 test curve is shown in purple with a better R^2 of 0.997. Twenty-one other spectra fall within the blue and red curves.

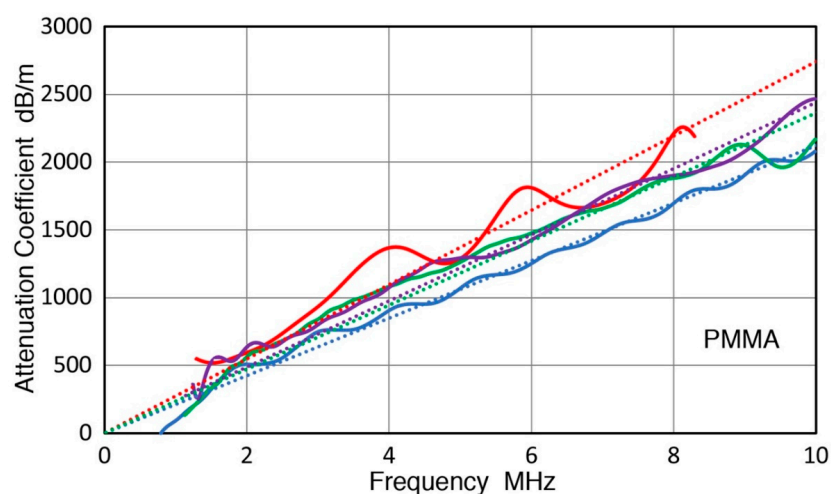


Figure 2. Transverse attenuation coefficient of polymethyl methacrylate (PMMA) vs. frequency. Three transmission difference method 1 (TDM-1) spectra for low, middle, and high C_{dt} values are shown by blue, green, and red curves, accompanied by their linear fits in dotted lines. One TDM-2 spectrum is plotted in purple.

Test results of transverse attenuation coefficients, α_t , of PMMA are tabulated in Table 1. All the data were fitted to the linear frequency dependence and the least-square fitted slopes of α_t vs. f curves, C_{dt} , are listed with R^2 values. The averages of TDM-1 and TDM-2 test results are $C_{dt} = 253.2$ and 238.6 dB/m/MHz, respectively. The TDM-2 result is 5% lower than the TDM-1 value. A similar difference was previously observed for the case of longitudinal attenuation coefficients of PMMA [13]. It was attributed to the T_c term requiring a correction. The observed C_{dt} of 253 ± 16.5 dB m/MHz from 17 TDM-1 tests agrees to that found in Simon et al. [37], within 6% of Tran et al. [35] and within 14% of the Hartmann-Jarzynski data [36]. The observed agreement of C_{dt} values indicates that the test methods used here, TDM-1 and TDM-2, can be used to estimate the transverse attenuation behavior of materials with an estimated error of $\pm 20\%$. This error estimate is taken to be three times higher than the best-case error of PMMA, considering typical attenuation tests used TDM-2 and sample conditions were less favorable.

Table 1. Test results of transverse attenuation coefficients, α_t , of PMMA.

Test Method	C_{dt}	R^2	v_t	Damping Factor	Thickness
	dB/m/MHz		mm/ μ s	η_t	mm
TDM-1	211	0.999	1.41	0.0109	17.95, 5.25
TDM-1	260	0.992	1.39	0.0132	17.8, 9.11
TDM-1	236	0.994	1.40	0.0121	9.11, 5.25
TDM-1	231	0.992	1.39	0.0118	17.8, 5.25
TDM-1	238	0.994	1.40	0.0122	9.11, 5.25
TDM-1	259	0.994	1.41	0.0134	17.95, 5.25
TDM-1	260	0.992	1.41	0.0134	17.95, 9.11
TDM-1	251	0.993	1.40	0.0129	11.75, 5.25
TDM-1	249	0.993	1.39	0.0127	27.3, 5.25
TDM-1	248	0.992	1.39	0.0126	27.3, 9.11
TDM-1	260	0.992	1.39	0.0132	27.3, 11.75
TDM-1	263	0.993	1.38	0.0133	24.64, 5.25
TDM-1	261	0.992	1.38	0.0132	24.64, 9.11
TDM-1	260	0.992	1.38	0.0131	24.64, 11.75
TDM-1	270	0.993	1.40	0.0139	24.77, 5.25
TDM-1	274	0.991	1.40	0.0141	24.77, 9.11
TDM-1	274	0.989	1.40	0.0141	24.77, 11.75
Average	253.2	0.9928	1.395	0.0129	
Std dev	16.5	0.0020	0.010	0.0008	
TDM-2	211	0.997	1.41	0.0109	17.95
TDM-2	240	0.997	1.39	0.0122	17.80
TDM-2	219	0.998	1.40	0.0112	9.11
TDM-2	244	0.997	1.41	0.0126	17.95
TDM-2	224	0.996	1.40	0.0115	11.75
TDM-2	253	0.996	1.39	0.0129	27.30
TDM-2	259	0.995	1.38	0.0131	24.64
TDM-2	259	0.995	1.40	0.0133	24.77
Average	238.6	0.9964	1.40	0.0122	
Std. dev.	18.6	0.0011	0.010	0.0009	
Quartz TDM-1	223	0.953	1.38	0.0113	9.11, 5.25

Std. dev.: Standard deviation.

PMMA transverse attenuation data was further separated into two parts. The first group (T1 through T11) is for plate thicknesses under 18 mm including T9 to T11 with 27.3-mm thickness, which were glued together from 9.1-mm plates. The second group (T12 to T17) used plates of nominally 25-mm thickness. The average values of C_{dt} were 245 and 269 dB/m/MHz for the two groups. Thicker plates showed about 10% higher α_t value. This difference appears to come from the internal stress of PMMA as thinner plates have higher residual stress from faster cooling during manufacturing. The damping factor of PMMA was shown to decrease with the applied stress [38].

Taking the average C_{dt} value of 253 dB/m/MHz to be representative, this is 2.8 times that of C_d value of 91.4 dB/m/MHz for the longitudinal waves. This ratio is larger than the inverse ratio of wave velocities of 1.6. The average transverse damping factor was 0.013, compared to 0.008 for the

longitudinal damping factor. The ratio of these two damping factors is 1.62 and matches well with the damping factor ratio at lower frequencies found in the literature. As reviewed in [13], the ratio was 1.6 from 0.2 to 20 kHz. Thus, the value of C_{dt} in this work and those of [35–37] fit the decreasing trend of PMMA damping with increased frequency. At the low MHz range, however, the damping factor becomes a constant, as indicated by the good linearity of α_t .

Table 1 also lists a representative result of C_{dt} measurements using quartz disk transducers. Two 9.5-mm diameter, AC-cut crystals of 5-MHz center frequency were bonded for through-transmission tests for the TDM-1 method using two thicknesses of PMMA plates. Linear fitting of the obtained spectrum was poor with $R^2 = 0.953$. C_{dt} was 20% lower than the average PMMA C_{dt} value. Due to a narrow high-sensitivity band, effects of spectral shifts made rational analysis difficult. Several other materials were tested similarly, but reproducibility was low. This reproducibility issue with the quartz tests was likely due to the lack of adequate forces that can be put in thin quartz disks as suitable solid bonding methods were unavailable. It appears that the puls \times echo mode with tuned excitation may be beneficial. Unfortunately, equipment break-down prevented further attempts with puls \times echo testing.

The transducer to sample coupling is crucial in contact testing. In the present work, ultrasonic gel couplant was used (type 54T04, Sonotech, Glenview, IL, USA) under force of 200–250 N (corresponding to the maximum torque that can be applied by two fingers on a 12-mm diameter bolt). This force (which is approximately 0.7 MPa) was 5–8 times higher than that needed to establish a good contact in longitudinal wave testing [13]. The time to reach the stabilized condition was 8 to 10 times longer, typically needing 4 to 5 h at 25 °C. All the testing was done at 25 ± 2 °C.

Having shown the consistency of transverse attenuation measurements using TDM-1 and TDM-2, testing of various materials is next conducted. In most cases, TDM-2 will be utilized. Whenever multiple samples are available, TDM-1 will supplement TDM-2. The general behavior of attenuation data will be described. Comparison among similar materials and between longitudinal and transverse wave attenuation behaviors will be made. Discussion on damping mechanisms will also be added where warranted.

3. Results and Discussion

3.1. Attenuation Behavior of Iron and Ferrous Alloys

Pure iron and 24 iron-base alloys were tested for transverse attenuation and the results are summarized in Table 2. TDM-2 was used for all the samples, and TDM-1 was also used for 1020 steel. The directional effects were evaluated for plate samples of 4340, HSLA, and 304 steels. Effects of cold work and heat treatment were also examined in some steels. In Table 2, attenuation coefficients of longitudinal and transverse modes are given to allow for the comparison between the two modes. Following the test number and material, values of C_d , C_R , v , C_{dt} , C_{Rt} , v_t , η , η_t , C_{dt}/C_d , η_t/η , sample thickness, Vickers hardness number (VHN), and notes are listed for each sample. The test number and attenuation data for the longitudinal mode tests are from Table 2 in reference [13], and additional longitudinal test results are also listed (marked by a suffix on the test number). Note that η and η_t are included in Table 2 since these represent the measure of dynamic viscosity as discussed in Section 1. These damping factors are rarely used for metallic materials, although Q^{-1} ($= \eta$) was used earlier in the internal friction studies of metals. However, this η and derived terms are widely used in various materials fields. The relevance of η and η_t can readily be seen in the first four lines of Table 2. For pure iron, $\eta = 0.028$ – 0.03 , which exceeds $\eta = 0.008$, found for a typical viscoelastic polymer, PMMA [13]. Transverse damping factor (η_t) of pure iron of 0.019 also exceeds that of PMMA ($\eta_t = 0.013$), given in Table 1. Seven steels, including T8 tool steel, 321 and A286 stainless steels, showed η values similar to or higher than that of PMMA, while only A286 steel exceeded η_t of PMMA. Thus, metallic materials should be considered as viscoelastic when η is larger than 0.005 to 0.008. Only a few exceptional solids such as fused silica may behave as purely elastic.

Table 2. Attenuation coefficients of longitudinal and transverse modes of iron and ferrous alloys.

Test.	Material	C _d	C _R	v	η	C _{dt}	C _{Rt}	v _t	η _t	C _{dt} /C _d	η _t /η	Thickness	Vickers	Notes
No		dB/m/ MHz	dB/m/ MHz ²	mm/ μs		dB/m/ MHz	dB/m/ MHz ²	mm/ μs				mm	HN	
F1	Pure Fe	129		6.05	2.86×10^{-2}	164		3.21	1.93×10^{-2}	1.271	0.675	72.1	174	Cold worked
F1a	Pure Fe	135		6.05	2.99×10^{-2}	164		3.21	1.93×10^{-2}	1.215	0.645	72.1	174	Cold worked
F2	Pure Fe	125.8		6.08	2.80×10^{-2}	159		3.28	1.91×10^{-2}	1.264	0.682	30.2	91	Annealed
F2a	Pure Fe	136		6.05	3.01×10^{-2}	159		3.28	1.91×10^{-2}	1.169	0.634	30.2	91	Annealed
F9	1020	9.8	1.41×10^{-2}	5.91	2.12×10^{-3}	15.6	3.13×10^{-2}	3.21	1.83×10^{-3}	1.592	0.865	31.8	100	Annealed
F10	1020	7.6	8.60×10^{-3}	5.87	1.63×10^{-3}	13.6	3.57×10^{-2}	3.21	1.60×10^{-3}	1.789	0.979	139.0	100	Annealed
F11	1020	7.5	5.74×10^{-3}	5.87	1.61×10^{-3}	11.1	4.35×10^{-2}	3.21	1.31×10^{-3}	1.480	0.809	31.8/139.0	100	Annealed TDM-1
F12	Low C steel	0	(4.84: n = 2)	5.93	1.05×10^{-3}	16.9	4.51×10^{-1}	3.26	2.02×10^{-3}	3.492	1.928	66.4	161	
F38	4340	6.0		5.86	1.29×10^{-3}	6.7		3.16	7.72×10^{-4}	1.112	0.599	61.0	315	
F39	4340 (T)	9.1		5.92	1.98×10^{-3}	6.3		3.21	7.45×10^{-4}	0.693	0.376	79.0	315	Same as F38
F40	4340 (S)	8.2		5.85	1.76×10^{-3}	22.6		3.22	2.67×10^{-3}	2.753	1.515	25.2	315	Same as F38
F44	4142	5.5	1.25×10^{-3}	5.92	1.18×10^{-3}	12.9		3.23	1.53×10^{-3}	2.367	1.291	60.3	321	Same as F42–F48
F44a	4142	5.5	1.25×10^{-3}	5.92	1.18×10^{-3}	15.8		3.23	1.87×10^{-3}	2.899	1.582	60.3	321	
F45	4142 (T)	25.5		5.75	5.37×10^{-3}	28.9		3.21	3.40×10^{-3}	1.133	0.633	18.9	321	
F51	4142 (T)	13.2		5.75	2.78×10^{-3}	14.1		3.19	1.65×10^{-3}	1.068	0.593	18.9	164	OQ + temper
F53	1060	15.3		5.93	3.32×10^{-3}	11.0	5.70×10^{-3}	3.24	1.31×10^{-3}	0.719	0.393	54.3	198	Rail steel
F58	HSLA-SM50	4.6		5.81	9.71×10^{-4}	13.0	2.13×10^{-3}	3.21	1.53×10^{-3}	2.851	1.575	75.0	132	Same as F59, F60
F59	HSLA-SM50 (T)	4.9		5.86	1.05×10^{-3}	12.9	1.54×10^{-3}	3.23	1.53×10^{-3}	2.633	1.451	71.2	132	
F60	HSLA-SM50 (S)	15.4		5.85	3.30×10^{-3}	12.5	2.59×10^{-3}	3.22	1.47×10^{-3}	0.812	0.447	50.1	132	
F66	A533B	7.1		5.91	1.53×10^{-3}	5.2	2.63×10^{-3}	3.23	6.11×10^{-4}	0.729	0.398	60.7	189	
F68	1Cr-1Mo-V	6.4		5.88	1.37×10^{-3}	5.9	3.28×10^{-3}	3.23	7.02×10^{-4}	0.931	0.511	60.8	240	
F72	Tool steel T8 (T)	56.7		5.75	1.19×10^{-2}	36.6		3.2	4.29×10^{-3}	0.646	0.359	12.7	1155	
F72a	Tool steel T8 (T)	66.9		5.87	1.44×10^{-2}	36.6		3.2	4.29×10^{-3}	0.547	0.298	12.7	1155	
F76	Hardness block4	28.4		5.92	6.16×10^{-3}	37.5		3.18	4.37×10^{-3}	1.320	0.709	14.8	847	
F79	301	9.4	1.47×10^{-3}	5.92	2.05×10^{-3}	13.2		3.25	1.57×10^{-3}	1.398	0.768	76.2	214	Magnetic
F79a	301	9.4	1.47×10^{-3}	5.92	2.05×10^{-3}	14.9	2.75×10^{-3}	3.25	1.77×10^{-3}	1.578	0.867	76.2	214	Magnetic
F82	302	18.6		5.87	4.00×10^{-3}	1.4	1.19×10^{-2}	3.08	1.34×10^{-6}	0.074	0.001	43.7	267	
F82a	302	11.4	4.11×10^{-3}	5.87	2.45×10^{-3}	1.4	1.19×10^{-2}	3.08	1.343×10^{-6}	0.120	0.000	43.7	267	
F84	302	4.03	1.00×10^{-3}	5.73	$[8.46 \times 10^{-4}]$	0	7.20×10^{-3}	3.1	$[8.18 \times 10^{-7}]$	0.002	0.001	77.4	279	Nonmagnetic
F84	302	42.2		5.7	8.81×10^{-3}	46.9		3.14	5.40×10^{-3}	1.111	0.612	10.5	228	Nonmagnetic
F85	304	1.5	1.10×10^{-3}	5.72	3.12×10^{-4}	0	4.85×10^{-3}	3.14	5.58×10^{-7}	0.003	0.002	479	321	Magnetic
F86	304	21.2	7.78×10^{-3}	5.75	4.47×10^{-3}	17.1	4.33×10^{-2}	3.14	1.97×10^{-3}	0.807	0.440	76.0	193	
F87	304 (T)	22.0	9.98×10^{-3}	5.72	4.61×10^{-3}	19.4	4.39×10^{-2}	3.14	2.23×10^{-3}	0.882	0.484	50.1	193	Same as F86
F88	304 (S)	38.2	8.92×10^{-3}	5.83	8.16×10^{-3}	10.1	4.99×10^{-2}	3.16	1.17×10^{-3}	0.264	0.143	19.0	193	Same as F86
F89	304L (S)	23.4	1.36×10^{-2}	5.65	4.84×10^{-3}	26.2	1.23×10^{-1}	3.16	3.03×10^{-3}	1.120	0.626	25.6	199	
F90	316	25.0	4.48×10^{-3}	5.69	5.21×10^{-3}	0	1.53×10^{-2}	3.14	1.76×10^{-6}	0.001	0.000	26.8	368	
F90a	316	11.9	2.33×10^{-3}	5.67	2.47×10^{-3}	0	1.90×10^{-2}	3.14	2.19×10^{-6}	0.002	0.001	26.8	368	

Table 2. Cont.

Test.	Material	C _d	C _R	v	η	C _{dt}	C _{Rt}	v _t	η _t	C _{dt} /C _d	η _t /η	Thickness	Vickers	Notes
No		dB/m/ MHz	dB/m/ MHz ⁴	mm/ μs		dB/m/ MHz	dB/m/ MHz ⁴	mm/ μs				mm	HN	
F91	321	55.8		5.78	1.18 × 10 ⁻²	23.4	2.20 × 10 ⁻²	3.16	2.71 × 10 ⁻³	0.419	0.229	34.0	196	
F91a	321	61.8		5.76	1.30 × 10 ⁻²	23.4	2.20 × 10 ⁻²	3.16	2.71 × 10 ⁻³	0.379	0.208	34.0	196	
F91b	321	49.1		5.83	1.05 × 10 ⁻²	23.4	2.20 × 10 ⁻²	3.16	2.71 × 10 ⁻³	0.477	0.258	34.0	196	
F94	430 (S)	9.9		5.81	2.10 × 10 ⁻³	9.13		3.13	1.05 × 10 ⁻³	0.924	0.498	24.3	312	
F94a	430 (S)	9.9		5.81	2.10 × 10 ⁻³	3.93	1.24 × 10 ⁻³	3.11	4.48 × 10 ⁻⁴	0.398	0.213	24.3	312	
F95	440A (S)	39.5		5.85	8.47 × 10 ⁻³	17.4		3.19	2.03 × 10 ⁻³	0.441	0.240	19.0	541	
F95a	440A (S)	31.4		5.83	6.71 × 10 ⁻³	17.4		3.19	2.03 × 10 ⁻³	0.554	0.303	19.0	541	
F102	A286 (S)	71.9	1.09 × 10 ⁻¹	5.75	1.51 × 10 ⁻²	142	6.46 × 10 ⁻¹	3.16	1.64 × 10 ⁻²	1.975	1.085	13.9	293	
F100	17-4PH	9.0	4.19 × 10 ⁻³	6.10	2.01 × 10 ⁻³	26.3		3.17	3.05 × 10 ⁻³	2.925	1.520	238.3	360	Solution treated
F100a	17-4PH	9.0	4.19 × 10 ⁻³	6.10	2.01 × 10 ⁻³	31.0		3.17	3.60 × 10 ⁻³	3.448	1.792	238.3	360	Solution treated
F101	17-4PH	34.7		5.84	7.43 × 10 ⁻³	53.4		3.17	6.20 × 10 ⁻³	1.539	0.835	25.4	412	Aged at 480 °C
F101a	17-4PH	30.2		5.86	6.67 × 10 ⁻³	31.3		3.19	3.75 × 10 ⁻³	1.194	0.647	25.4	412	Aged at 480 °C
I3	Gray class 20	0	(35.0: n = 2)	4.47	[5.73 × 10 ⁻³]	0	(82.0: n = 2)	2.47	[7.42 × 10 ⁻³]	2.343	1.295	25.0	145	As-cast
I8	Gray class 60	0	(18.7: n = 2)	5.00	[3.43 × 10 ⁻³]	0	(32.66: n = 2)	2.79	[3.34 × 10 ⁻³]	1.747	0.973	24.8	242	As-cast
I18	Ductile 80-55-06	41.0	8.38 × 10 ⁻³	5.64	8.47 × 10 ⁻³	80.0	0.0439	3.12	9.15 × 10 ⁻³	1.951	1.079	25.0	282	As-cast
I21	Malleabl × ferritic Average	28.5	7.90 × 10 ⁻³	5.52	5.76 × 10 ⁻³	83.3	0.0125	3.08	9.40 × 10 ⁻³	2.923	1.631	24.0	145	Heat treated
					6.69 × 10 ⁻³				3.97 × 10 ⁻³					

OQ: Oil quenched.

When one examines the values of the ratio, C_{dt}/C_d , as well as C_d and C_{dt} on Table 2, 43% of the tests showed lower C_{dt} than C_d , (or $C_{dt}/C_d < 0.67$), while 40% had comparable C_{dt} with C_d ($0.67 \leq C_{dt}/C_d < 1.5$) with the remaining 17% had C_{dt} 1.5-times or higher than C_d ($1.5 \leq C_{dt}/C_d$). The average of C_{dt}/C_d values was 1.19 and 50% of the tests resulted in $0.5 < C_{dt}/C_d < 1.5$. This distribution differed from an expectation of much higher C_{dt} over the entire tests. This expectation came from the previous transverse attenuation results of metals and polymers, reviewed in [13], and Q values of rocks and the Earth [1,6]. The ratio of damping factors, η_t/η , was smaller than C_{dt}/C_d ratios, with their average equaling 0.65 and only 20% exceeded unity ratio. The observed similarities of η and η_t values for a given sample are consistent with the dislocation bow-out mechanism of damping, proposed in [13].

Structural steels from 1020 to 1Cr-1Mo-V turbine rotor steels in Table 2 showed low transverse attenuation with C_{dt} values below 20 dB/m/MHz except for two cases. These were modestly higher than the corresponding C_d values. C_{dt} values for high alloy steels were higher, but most of them were less than 50 dB/m/MHz. Of these, A286 steel showed exceptionally high C_d and C_{dt} values of 72 and 142 dB/m/MHz (note that previous results for A286 steels had to be moved to the Ni-base alloy category due to mislabeling. This A286 sample is a new addition.) The 300-series austenitic stainless steels exhibited slightly higher attenuation than low alloy steels, but cold working reduced transverse attenuation to low levels as was the case for longitudinal attenuation (see Tests F84, F85, F90). These three cold-worked stainless steels showed no damping term ($C_{dt} = 0$) and the transverse attenuation, α_t , followed a 4th-power frequency dependence, indicating Rayleigh scattering. Another cold-worked 302 stainless steel (Test F83) with lower hardness showed the usual Mason-McSkimin relation, but also with low C_{dt} value of 1.4 dB/m/MHz.

The Mason-McSkimin relation that includes the 4th-power frequency dependent term was found in more cases for transverse attenuation. The coefficient, C_{Rt} , was always higher than the corresponding C_R term of the same sample. The increase was 9-fold in 304L stainless steel (Test F89), and 7.5-fold in 1020 steel (Test F11), while C_{Rt} appeared in some steels for which C_R was absent (HSLA, A533B, 1Cr-1Mo-V steels, and 321 stainless steel, Tests F58, F66, F68, F91). Figure 3 shows a comparison of the longitudinal and transverse attenuation spectra of 1020 steel (Test F11). The initial slopes differed only 50%, but the two curves diverged with increasing frequency. Three samples showed especially high scattering effects. These were A286 and 304 stainless steels in the thickness direction and a low-C steel (Tests F99a, F89, F12). Both stainless samples had large C_R values also. The low-C steel sample (Test F12) showed a frequency-squared dependence previously, which now appears to come from scattering as in the case of transverse attenuation. Observed results in steels indicate that the scattering effects of transverse waves are stronger from grain boundaries, second phases, and non-metallic inclusions.

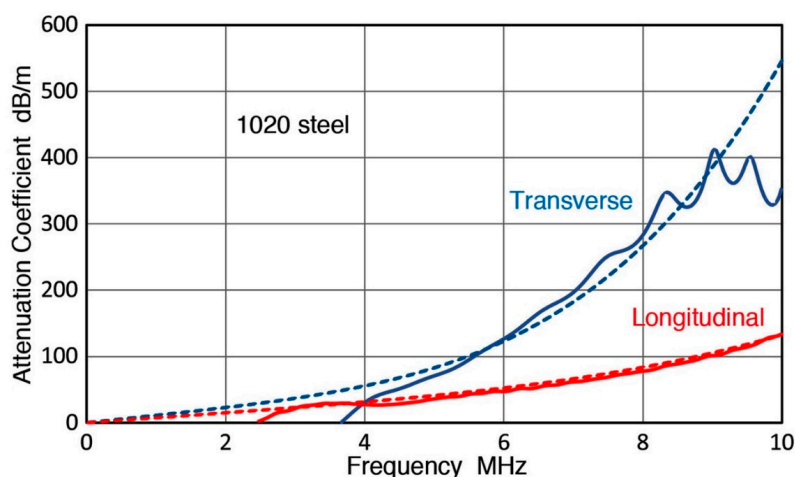


Figure 3. Attenuation coefficients vs. frequency. Transverse attenuation spectrum of 1020 steel is plotted in blue curve with the Mason-McSkimin fitted dashed curve. Corresponding longitudinal attenuation spectrum from [13] is shown in red, also with the Mason-McSkimin fitted dashed curve.

The transverse attenuation spectra of six austenitic stainless steels are compared in Figure 4. These include Type 301 (blue curve), 302 (red), 304 (purple), 304L (dark red), 316 (dark blue), and 321 (green). Of these steels, 301 had nearly linear spectrum with the lowest scattering, while 304L showed the strongest Rayleigh scattering. Type 316 (in cold-worked condition) only had the scattering term. In all cases, the transverse attenuation was moderate below 5 MHz.

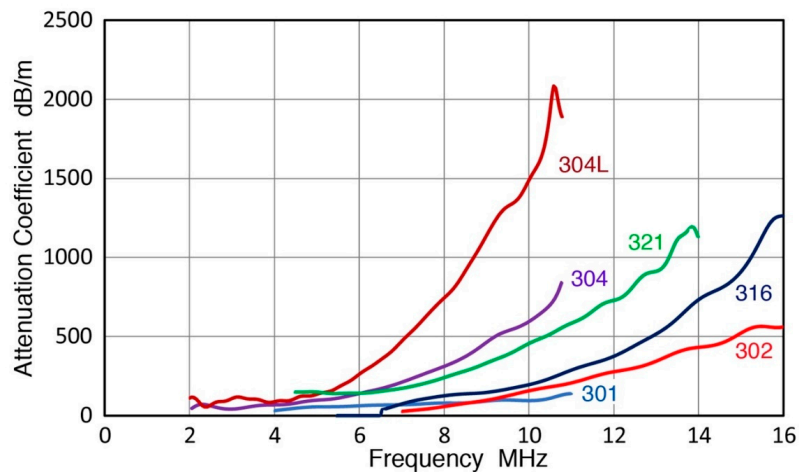


Figure 4. Transverse attenuation coefficients vs. frequency for six austenitic stainless steels. The attenuation spectra of five stainless steels fitted to Mason-McSkimin relations are plotted in dark red (304L), purple (304), green (321), dark blue (316), and red (302), respectively. The 301 stainless steel showed a linear spectrum, given in blue.

Two high hardness steels (T8 tool steel and a hardness block, Tests F72 and F76) showed moderate levels of C_{dt} values (37–38 dB/m/MHz), which were lower for T8 and higher for the block than their respective C_d values. Their high hardness conditions (VHN of 1155 and 847) reflect dispersed carbides and martensitic microstructures that impede dislocation motion. Yet, their damping is higher than much softer cold-worked 302 and 304 stainless steels (VHN of 362 and 321). This remains to be a topic for further study.

Anisotropic directionality effects observed in longitudinal attenuation were examined for three steel plates of 4340, HSLA, and 304 (Tests F38–40, F58–60, F86 = 88). Previously, the thickness (S) direction showed the highest (or next highest) attenuation. For transverse attenuation, the same behavior was only found in the 4340 plate, for which C_{dt} for the S direction was more than three times higher than either the longitudinal (L) or transverse (T) direction. In the L or T direction, C_{dt} was comparable to C_d . In the HSLA steel plate, C_{dt} showed no directionality as three values were essentially identical. Spectral responses of this hot-rolled HSLA steel block (JIS-SM50 grade, Nippon Kokan, Kawasaki, Japan: 0.15% C, 0.29 Si, 1.29 Mn) are shown in Figure 5. The purple and light green curves represent α term of the longitudinal (L) and short-transverse (S) orientations without scattering contributions. The transverse attenuation spectra in the three orientations are plotted in blue (L), red (transverse or T), and green (S) curves, each with some scattering effects. The spread of these three α_t curves are smaller than the two for α . In contrast, an opposite anisotropic effect was found in the 304 stainless steel plate. That is, the S direction showed the lowest attenuation. The scattering contribution was similar in the three directions in both wave modes. Since the microstructures varied in these plates (tempered bainitic, ferritic-pearlitic, and annealed austenitic, respectively), no clear cause can be suggested for the observed results. However, directionality effects need to be considered when one needs to utilize published attenuation data.

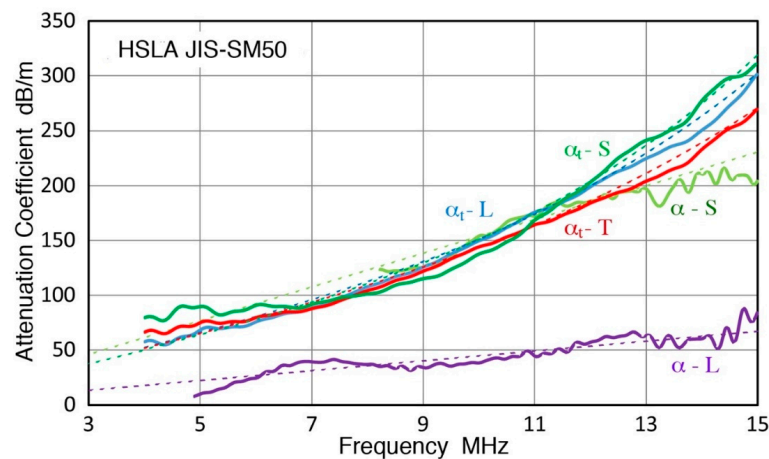


Figure 5. Anisotropic transverse attenuation (α_t) spectra of a high-strength low alloy steel plate with curve fitting. Blue: Longitudinal (L) direction; red: Transverse (T) direction; green: Thickness (S) direction. Longitudinal attenuation (α) spectra are shown in comparison. Purple: Transverse direction; light green: Thickness direction.

Previously published transverse attenuation (α_t) data is limited, but two cases may be compared. Hirao et al. [39,40] used a resonance method with an electromagnetic transducer and obtained α_t values of 0.15% C and 1Cr-1Mo-V steels at 5 MHz. Converting the data, their C_{dt} values became 23.2 and 6.6 dB/m/MHz. These can be compared to C_{dt} values of a low-C steel (Test F12) and 1Cr-1Mo-V steel (Test F68), which are 16.9 and 5.9 dB/m/MHz. These are in good agreement.

A separate part of Table 2, the last four rows, provide the attenuation data of four cast iron samples. These represent three types of cast iron, gray, ductile, and malleable. Test I3 was on gray cast iron of class 20, which is of the lowest strength grade (minimum tensile strength of 150 MPa). Test I8 was on class 60 gray iron (minimum tensile strength of 430 MPa). Test I18 was on ductile iron 80-55-06 grade (minimum tensile strength of 552 MPa). Test I21 was on ferritic malleable iron. The transverse attenuation spectra of these four samples are plotted in Figure 6. Gray iron showed attenuation with frequency-squared dependence for both longitudinal and transverse modes, but the attenuation coefficients were about twice larger in the transverse mode. The steeply rising blue curve is for class 20 gray iron and the next red curve is for class 60 gray iron. Ductile iron (grade 80-55-06: Green curve) and ferritic malleable iron (purple) showed the Mason-McSkimin relation for the transverse mode. The same relation was found previously for the longitudinal mode. The transverse attenuation coefficients for the ductile and malleable irons were 2 to 2.9 times higher than their longitudinal counterparts. As was the case in steels, the ratio of damping factors, η_t/η , was smaller than the C_{dt}/C_d ratios since the η_t/η ratio factors in the velocity ratio of less than unity.

The frequency-squared dependence in gray iron was attributed to two mechanisms in [13]. One was due to multiple scattering according to the Datta-Kinra theory [17]. Another proposed mechanism was based on the reflection from rough surfaces [41]. In both explanations, the transverse wave scattering or reflection needs to be stronger. It is unclear how such changes can be produced. The increased damping terms in the transverse attenuation of ductile iron and ferritic malleable iron actually give η_t/η ratios closer to unity. Thus, dislocation damping due to bow-out [13] can account for the difference.

It is noted here that gray irons have ultrasonic attenuation comparable or lower than ductile or malleable iron below 1 MHz. This is opposite to the vibration damping behavior of these materials [42]. At sub-kHz frequencies, gray irons have more than ten-fold increase in damping. The main source of the contrary behavior comes from much higher vibration amplitudes at low frequencies, introducing frictional damping processes at graphite flakes.

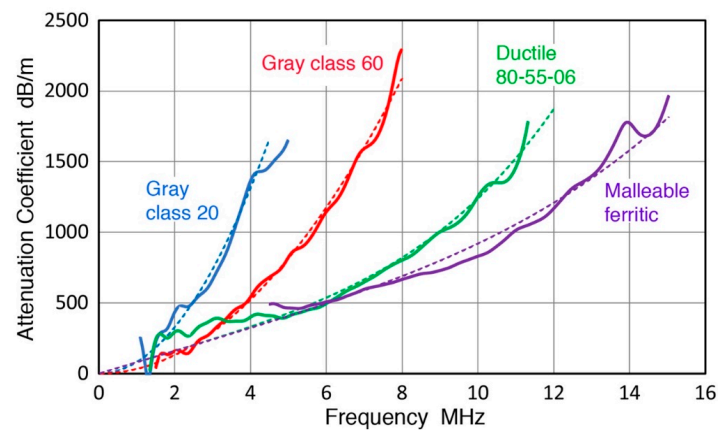


Figure 6. Transverse attenuation spectra of gray irons, class 20 and 60, ductile iron (grade 80-55-06) and ferritic malleable iron are plotted in blue, red, green, and purple curves. Gray iron curves were fitted to frequency-squared relations, while ductile and malleable irons to Mason-McSkimin relations. Fitted relations are given in dashed curves.

3.2. Attenuation Behavior of Non-Ferrous Metals and Alloys

Four pure metals and 23 non-ferrous alloys were evaluated for transverse attenuation and the results are summarized in Table 3. This table has the same format as Table 2. Four new material types (electroformed Cu, single crystal Ni₃Al, Inconel 600 and 738) were added, for which longitudinal attenuation tests were also conducted. TDM-2 was used for all the samples, and TDM-1 was also used for four tests of Al6061, Mg, and Mg AZ61. Generally, the transverse attenuation coefficient was higher than the corresponding longitudinal attenuation coefficient in contrast to the ferrous alloy behavior discussed in Section 3.1. About one half (51%) of the attenuation spectra showed the linear frequency dependence, while 38% followed the Mason-McSkimin relation with Rayleigh scattering term. The remaining 11% showed frequency-squared (and -cubed) dependence, although most of these spectra can also be fitted to the Mason-McSkimin relation. These nine test results are double listed in Table 3.

Aluminum alloys, including 2011, 2014, 2024, 6061, 7049, and 7075 alloys, showed low transverse attenuation, giving C_{dt} in the range of 3 to 34 dB/m/MHz. This is roughly twice the corresponding C_d range of 1.4 to 15 dB/m/MHz, but individual C_{dt}/C_d ratios varied from 1.5 to 10.5. Another difference from the longitudinal mode was that the large C_{dt} was more often found with T6 conditions. This observation adds one more issue in trying to understand the attenuation of Al alloys since aluminum is isotropic in the elastic behavior. Since scattering effects depend on the mean square variation of elastic constants [2,16,43], Rayleigh scattering ought to be small regardless of wave modes.

Copper single crystal in the <111> orientation showed 1.8-times higher attenuation in the transverse mode, but no scattering term was observed as expected from the absence of grain boundaries. Its C_{dt} values were 1.3× to 2× higher than the slightly harder polycrystalline Cu samples (Tests N28, N30). A similarly soft electroformed Cu (Test N102) showed almost twice higher C_d and the transverse attenuation with the frequency-squared dependence of α_t , giving much lower α_t values below 2 MHz.

Table 3. Attenuation coefficients of longitudinal and transverse modes of non-ferrous metals and alloys.

Test.	Material	C _d	C _R	v	η	C _{dt}	C _{Rt}	v _t	η _t	C _{dt} /C _d	η _t /η	Thickness	Vickers	Notes
No		dB/m /MHz	dB/m /MHz ⁴	mm/μs		dB/m /MHz	dB/m /MHz ⁴	mm /μs				mm	HN	
N1	Al 2011	6.4		6.23	1.45 × 10 ⁻³	21.0	3.90 × 10 ⁻³	3.1	2.39 × 10 ⁻³	3.31	1.65	48.1	103	
N2	Al 2011	1.4	5.60 × 10 ⁻³	6.25	3.18 × 10 ⁻⁴	9.0	8.11 × 10 ⁻³	3.12	1.03 × 10 ⁻³	6.47	3.23	135.0	155	T6 temper
N3	Al 2014	5.6	1.90 × 10 ⁻³	6.35	1.30 × 10 ⁻³	16.8	9.28 × 10 ⁻³	3.12	1.92 × 10 ⁻³	3.00	1.47	69.2	155	T6 temper
N100	Al 2014 (T)	4.9		6.32	1.13 × 10 ⁻³	21.7		3.15	2.50 × 10 ⁻³	4.43	2.21	50.7	155	Extrusion
N4	Al 2014	3.2	8.80 × 10 ⁻³	6.32	7.41 × 10 ⁻⁴	33.6		3.13	3.85 × 10 ⁻³	10.50	5.20	45.2	145	
N4a	Al 2014	5.3	4.47 × 10 ⁻²	6.28	1.21 × 10 ⁻³	24.5	1.41 × 10 ⁻²	3.12	2.80 × 10 ⁻³	4.64	2.31	34.1	149	
N7	Al 2024	1.7	1.49 × 10 ⁻³	6.36	4.03 × 10 ⁻⁴	3.1	3.09 × 10 ⁻³	3.10	3.56 × 10 ⁻⁴	1.81	0.88	154.2	170	T3 temper
N9	Al 2024	6.8		6.35	1.58 × 10 ⁻³	30.2		3.13	3.46 × 10 ⁻³	4.44	2.19	45.8	162	T851 temper
N10	Al 6061	4.0		6.38	9.44 × 10 ⁻⁴	34.8		3.23	4.12 × 10 ⁻³	8.61	4.36	31.0	109	T6 temper
N13	Al 2024	6.5		6.35	1.51 × 10 ⁻³	21.7	4.68 × 10 ⁻³	3.17	2.52 × 10 ⁻³	3.34	1.67	50.7	153	N8 annealed
N14	Al 6061	14.4		6.35	3.35 × 10 ⁻³	25.1		3.20	2.94 × 10 ⁻³	1.74	0.88	212.0	78	Annealed
N15	Al 6061	14.4		6.35	3.35 × 10 ⁻³	28.5		3.20	3.34 × 10 ⁻³	1.98	1.00	212/10.6	78	Annealed TDM-1
N17	Al 7049	6.9		6.21	1.57 × 10 ⁻³	16.2	5.59 × 10 ⁻³	3.06	1.82 × 10 ⁻³	2.35	1.16	45.8	128	T7 temper
N19	Al 7075	5.7		6.25	1.31 × 10 ⁻³	12.2		3.10	1.39 × 10 ⁻³	2.14	1.06	75.0	180	T6 temper
N20	Al 7075 (T)	5.9		6.26	1.35 × 10 ⁻³	10.6		3.08	1.20 × 10 ⁻³	1.80	0.88	76.0	180	Same as N19
N21	Al 7075 (S)	10.8		6.23	2.47 × 10 ⁻³	18.8		3.08	2.12 × 10 ⁻³	1.74	0.86	37.2	180	Same as N19
N101	Al 7075	15.1		6.3	3.49 × 10 ⁻³	22.3		3.10	2.53 × 10 ⁻³	1.48	0.73	45.8	201	T6 temper
N26	Cu single crystal	133		5.16	2.51 × 10 ⁻²	232		2.15	1.82 × 10 ⁻²	1.74	0.73	12.4	69.6	<111> Direction
N102	Cu	245		4.68	4.20 × 10 ⁻²		(83.45: n=2)	2.37	7.25 × 10 ⁻³	[0.34]	[0.17]	5.1	66.3	Electroformed
N28	OFHC Cu	25.3		4.47	4.14 × 10 ⁻³	116		2.91	1.24 × 10 ⁻²	4.58	2.98	81.5	77.6	
N28	OFHC Cu	25.3		4.47	4.14 × 10 ⁻³	174		2.92	1.86 × 10 ⁻²	6.88	4.49	19.8	77.6	
N28	OFHC Cu	25.3		4.47	4.14 × 10 ⁻³	150		2.92	1.60 × 10 ⁻²	5.93	3.87	1.57	77.6	
N30	Cu 110	41.6		4.64	7.07 × 10 ⁻³	88.4		2.40	7.77 × 10 ⁻³	2.13	1.10	51.5	100	
N32	Cu 110	43.5		4.67	7.44 × 10 ⁻³	176		2.46	1.59 × 10 ⁻²	4.05	2.13	34.6	77	Annealed
N33	Cu 110	0	(6.05: n = 2)	4.7	1.04 × 10 ⁻³	32.0	4.89 × 10 ⁻¹	2.26	2.65 × 10 ⁻³	[5.29]	2.54	48.5	99	
N34	Cu 110 (S)	35.4	1.30 × 10 ⁻²	4.57	5.93 × 10 ⁻³	77.1	3.30 × 10 ⁻¹	2.22	6.27 × 10 ⁻³	2.18	1.06	12.7	99	Same as N33
N35	Cu 110	0	(15.5: n = 2)	4.73	2.69 × 10 ⁻³	134	1.34	2.53	1.24 × 10 ⁻²	[8.65]	4.62	23.5	54.1	Annealed
N35	Cu 110	0	(15.5: n = 2)	4.73	2.69 × 10 ⁻³	0	(50.2: n = 2)	2.53	4.65 × 10 ⁻³	[3.24]	1.73	23.5	54.1	Annealed
N36	Cu 110 (S)	66.9	1.73 × 10 ⁻²	4.62	1.13 × 10 ⁻³	130	1.19	2.25	1.07 × 10 ⁻²	1.94	0.95	12.7	54.1	Same as N35
N36	Cu 110 (S)	66.9	1.73 × 10 ⁻²	4.62	1.13 × 10 ⁻³		(55.0: n = 2)	2.25	4.53 × 10 ⁻³	[0.82]	0.40	12.7	54.1	Same as N35
N37	Cu 110	10.1	8.47 × 10 ⁻²	4.72	1.75 × 10 ⁻³	89.2		2.24	7.32 × 10 ⁻³	8.83	4.19	49.5	86.1	
N41	Brass 260	0	(4.5: n = 2)	4.55	7.50 × 10 ⁻³		(2.695: n = 3)	2.21	2.19 × 10 ⁻⁴	[0.60]	0.29	95.0	91	
N42	Brass 260 (T)	0	(5.13: n = 2)	4.54	8.53 × 10 ⁻³	14.8	3.88 × 10 ⁻¹	2.21	1.20 × 10 ⁻³	[2.88]	1.40	90.3	91	
N42	Brass 260 (T)	0	(5.13: n = 2)	4.54	8.53 × 10 ⁻³		(2.556: n = 3)	2.21	2.07 × 10 ⁻⁴	[0.50]	0.24	90.3	91	
N43	Brass 260 (S)	60.2	2.84 × 10 ⁻²	4.49	9.90 × 10 ⁻³	74.7	2.63 × 10 ⁻¹	2.22	6.08 × 10 ⁻³	1.24	0.61	19.0	91	
N44	Brass 260	42.1	3.28 × 10 ⁻²	4.52	6.97 × 10 ⁻³	40.4	2.61 × 10 ⁻¹	2.22	3.29 × 10 ⁻³	0.96	0.47	45.8	85.8	Annealed
N44	Brass 260	42.1	3.28 × 10 ⁻²	4.52	6.97 × 10 ⁻³		(14.98: n = 2)	2.22	1.22 × 10 ⁻³	[0.36]	0.17	45.8	85.8	Annealed
N45	Brass 260 (S)	58.9	2.92 × 10 ⁻²	4.53	9.78 × 10 ⁻³	60.5	2.63 × 10 ⁻¹	2.22	4.92 × 10 ⁻³	1.03	0.50	19.0	85.8	Same as N44
N103	Brass 260	35.1	3.15 × 10 ⁻²	4.54	5.84 × 10 ⁻³	32.6	2.64 × 10 ⁻¹	2.22	2.65 × 10 ⁻³	0.93	0.45	56.8	122	
N103a	Brass 260	35.1	3.15 × 10 ⁻²	4.54	5.84 × 10 ⁻³		(13.04: n = 2)	2.22	1.06 × 10 ⁻³	[0.37]	0.18	56.8	122	

Table 3. Cont.

Test.	Material	C _d	C _R	v	η	C _{dt}	C _{Rt}	v _t	η _t	C _{dt} /C _d	η _t /η	Thickness	Vickers	Notes
No		dB/m /MHz	dB/m /MHz ²	mm/μs		dB/m /MHz	dB/m /MHz ²	mm /μs				mm	HN	
N46	Brass 280	0	(7.97: n = 2)	4.28	1.25 × 10 ⁻³	152		2.32	1.29 × 10 ⁻²	[19.07]	10.34	52.6	177	
N46	Brass 280	0	(8.31: n = 2)	4.3	1.31 × 10 ⁻³	152		2.32	1.29 × 10 ⁻²	[18.29]	9.87	52.6	177	
N104	Brass 360	27.0	1.21 × 10 ⁻²	4.36	4.31 × 10 ⁻³	36.5	8.10 × 10 ⁻²	2.18	2.92 × 10 ⁻³	1.35	0.68	49.3	109	
N104a	Brass 360	27.0	1.21 × 10 ⁻²	4.36	4.31 × 10 ⁻³	0	(8.9: n = 2)	2.18	7.11 × 10 ⁻⁴	[0.33]	0.16	49.3	109	
N58	Brass 360	31.5		4.36	5.03 × 10 ⁻³	62.1	3.15 × 10 ⁻²	2.17	4.94 × 10 ⁻³	1.97	0.98	31.7	97.5	
N62	Cu-Zr	56.7	4.03 × 10 ⁻²	4.69	9.74 × 10 ⁻³	0	(25.88: n = 2)	2.43	2.30 × 10 ⁻³	[0.46]	0.24	33.5	88.9	
N63	Cu-Al2O3	23.3		4.55	3.88 × 10 ⁻³	41.4		2.44	3.70 × 10 ⁻³	1.78	0.95	43.0	97.8	
N64	Cu-Al2O3	19.0		4.54	3.16 × 10 ⁻³	12.1	1.11 × 10 ⁻²	2.42	1.07 × 10 ⁻³	0.64	0.34	51.0	110	
N65	Cu-Ag-Zr	24.2	8.91 × 10 ⁻³	4.75	4.21 × 10 ⁻³	91.3		2.38	7.96 × 10 ⁻³	3.77	1.89	35.9	110	
N66	Pure Mg	6.6		5.81	1.40 × 10 ⁻³	15.6		3.12	1.78 × 10 ⁻³	2.37	1.27	160.0	40.5	99.95%
N66a	Pure Mg	4.9		5.8	1.03 × 10 ⁻³	15.6		3.12	1.78 × 10 ⁻³	3.20	1.72	160.0	40.5	99.95%
N67	Pure Mg	5.3		5.81	1.14 × 10 ⁻³	22.0		3.12	2.52 × 10 ⁻³	4.12	2.21	76	40.5	99.95%
N68	Pure Mg	4.4		5.82	9.28 × 10 ⁻⁴	11.1		3.12	1.27 × 10 ⁻³	2.55	1.37	76/160	40.5	99.95% TDM-1
N68a	Pure Mg	4.1		5.8	8.71 × 10 ⁻⁴	11.1		3.12	1.27 × 10 ⁻³	2.71	1.46	7.0/160	40.5	99.95% TDM-1
N69	Mg AZ61	2.0		5.75	4.19 × 10 ⁻⁴	4.0		2.99	4.38 × 10 ⁻⁴	2.02	1.05	100.6	91.4	
N69a	Mg AZ61	3.0		5.76	6.32 × 10 ⁻⁴	4.0		2.99	4.38 × 10 ⁻⁴	1.33	0.69	165.0	91.4	
N69b	Mg AZ61	4.4		5.76	9.22 × 10 ⁻⁴	4.0		2.99	4.38 × 10 ⁻⁴	0.92	0.48	35.3/165.0	91.4	TDM1
N70	Ni 200	60.4	2.60 × 10 ⁻²	5.72	1.27 × 10 ⁻²	301		2.97	3.28 × 10 ⁻²	4.98	2.59	46.0	115	No magnet
N70a	Ni 200	59.0	2.90 × 10 ⁻²	5.72	1.24 × 10 ⁻²	301		2.97	3.28 × 10 ⁻²	5.10	2.65	46.0	115	No magnet
N70b	Ni 200	48.0	3.25 × 10 ⁻²	5.72	1.01 × 10 ⁻²	140		3.05	1.56 × 10 ⁻²	2.92	1.56	46.0	115	* 1, * 2
N70c	Ni 200	31.5	2.82 × 10 ⁻²	5.76	6.65 × 10 ⁻³	140		3.05	1.56 × 10 ⁻²	4.44	2.35	46.0	115	* 2, * 3
N72b	Ni 200	20.4		5.77	4.31 × 10 ⁻³	21.1	5.78 × 10 ⁻³	3.08	2.38 × 10 ⁻³	1.03	0.55	38.0	234	* 4
N72c	Ni 200	18.3		5.77	3.87 × 10 ⁻³	21.1	5.78 × 10 ⁻³	3.08	2.38 × 10 ⁻³	1.15	0.62	38.0	234	* 5
N75	Monel 400	34.0		5.47	6.81 × 10 ⁻³	20.3	7.75 × 10 ⁻³	2.77	2.06 × 10 ⁻³	0.60	0.30	36.8	275	
N105	Inconel 600 (S)	86.6		6.35	2.01 × 10 ⁻²	139		3.76	1.92 × 10 ⁻²	1.61	0.95	11.2	322	
N106	Inconel 600 (S)	89.3		6.44	2.11 × 10 ⁻²	174		3.76	2.40 × 10 ⁻²	1.95	1.14	11.2	322	
N77	Inconel 625	15.5	1.08 × 10 ⁻²	5.83	3.31 × 10 ⁻³	21.1	6.05 × 10 ⁻²	3.08	2.38 × 10 ⁻³	1.36	0.72	46.2	317	
N77	Inconel 625	15.5	1.08 × 10 ⁻²	5.83	3.31 × 10 ⁻³	32.5	5.83 × 10 ⁻²	3.09	3.68 × 10 ⁻³	2.10	1.11	46.2	317	
N79	Inconel 718	21.9	1.67 × 10 ⁻¹	5.73	4.60 × 10 ⁻³	78.8		3.06	8.84 × 10 ⁻³	3.60	1.92	101.3	152	
N80	Inconel 718 (S)	56.3	1.83 × 10 ⁻¹	5.82	1.20 × 10 ⁻²	179	7.84 × 10 ⁻¹	3.04	1.99 × 10 ⁻²	3.18	1.66	14.2	152	
N107	Inconel 718	14.6	3.08 × 10 ⁻³	5.79	3.10 × 10 ⁻³	8.5	3.93 × 10 ⁻²	3.03	9.47 × 10 ⁻⁴	0.58	0.31	152.5	460	
N107a	Inconel 718	15.7	2.22 × 10 ⁻³	5.79	3.33 × 10 ⁻³	8.5	3.93 × 10 ⁻²	3.03	9.47 × 10 ⁻⁴	0.54	0.28	152.5	460	
N108	Inconel 738	18.5	1.57 × 10 ⁻¹	5.72	3.88 × 10 ⁻³	73.9		3.08	8.34 × 10 ⁻³	3.99	2.15	101.5	319	
N108	Inconel 738	0	(13.35: n = 2)	5.72	[2.80 × 10 ⁻³]	73.9		3.08	8.34 × 10 ⁻³	5.54	2.98	101.5	319	
N109	Inconel 738 (T)	41.6	1.25 × 10 ⁻¹	5.73	8.73 × 10 ⁻³	43.1	9.25 × 10 ⁻¹	3.12	4.93 × 10 ⁻³	1.04	0.56	46.4	319	
N110	Inconel 738 (S)	98.7	7.88 × 10 ⁻²	5.62	2.03 × 10 ⁻²	110	5.91 × 10 ⁻¹	3.12	1.26 × 10 ⁻²	1.11	0.62	15.2	319	
N110a	Inconel 738 (S)	66.7	9.98 × 10 ⁻²	5.62	1.37 × 10 ⁻²	153	5.99 × 10 ⁻¹	3.11	1.74 × 10 ⁻²	2.29	1.27	15.0	319	
N111	Ni ₃ Al	185		5.53	3.74 × 10 ⁻²	341		3.29	4.11 × 10 ⁻²	1.85	1.10	4.38	268	
N85	Ti-6-4	38.5		6.11	8.62 × 10 ⁻³	39.2	5.52 × 10 ⁻²	3.10	4.45 × 10 ⁻³	1.02	0.52	21.8	330	
N87	Ti-6-6-2	14.5	4.30 × 10 ⁻³	6.02	3.20 × 10 ⁻³	31.5		3.04	3.51 × 10 ⁻³	2.17	1.10	117.3	359	
N93	W	13.3		5.23	2.55 × 10 ⁻³	11.9		2.86	1.25 × 10 ⁻³	0.89	0.49	75.0	299	
Average						6.52 × 10 ⁻³						7.28 × 10 ⁻³		

* 1: Two magnets on sample in the longitudinal test; * 2: Three magnets on sample in the transverse test; * 3: Three magnets on sample in the longitudinal test; * 4: Cold worked sample without magnets; * 5: Cold worked sample with two magnets.

Figure 7 shows three types of transverse attenuation spectra observed in Cu and its alloys; linear (blue curve, Test N63), Mason-McSkimin (red, N64), and frequency-squared (green, N62). A peculiar feature of the longitudinal attenuation of Cu and brass was the prevalence of the frequency-squared dependence of attenuation coefficient, α . This behavior also exists in the transverse mode. In addition to Cu and brass, the frequency-squared dependence also appeared in a Cu-Zr alloy and Inconel 718, as well as frequency-cubed dependences in C260 (cartridge) brass (Tests N41, N42). Most of these square \times or cube \times dependences can be fitted to the Mason-McSkimin relation, which combines low damping and large Rayleigh scattering terms. In all cases with a good power-law fit, their elastic anisotropy is high and grain boundary scattering is strong. No Al alloys and steels exhibited the frequency-squared dependence out of ~ 140 tests. Finding Al and steels in the same group is strange as Al is isotropic but steels are not. Additional studies are needed to ascertain whether the power-law behaviors truly represent the attenuation of these alloys, especially by varying microstructures and cold working.

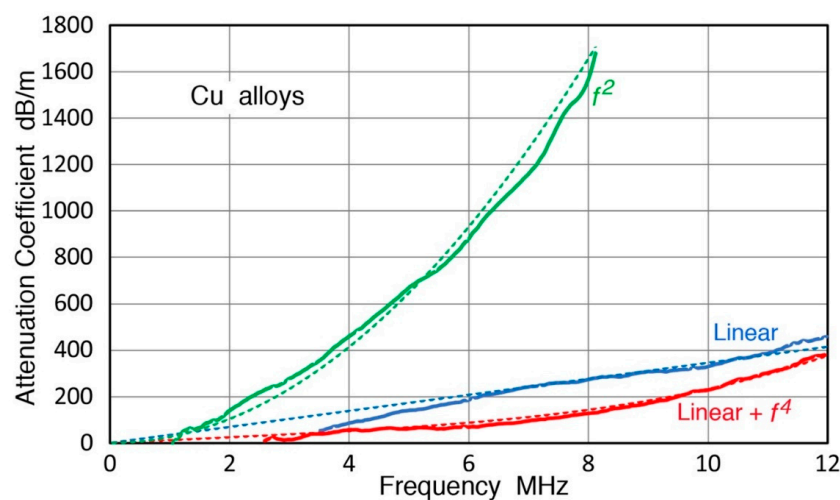


Figure 7. Three types of transverse attenuation spectra observed in Cu and its alloys: Linear (blue curve), Mason-McSkimin (red), and frequency-squared (green).

Comparison of different Cu and its alloys can be made when C_{dt} values can be assigned with the linear or Mason-McSkimin spectra. In OFHC Cu, C110 Cu (tough pitch grade) and C260 brass, annealed conditions generally produced high attenuation of more than 100 dB/m/MHz. Two-phase C280 brass also had high C_{dt} values. With cold working or with second phase additions, C_{dt} values decreased, sometimes down to the level comparable to the corresponding C_d values.

Both pure Mg and AZ61 Mg alloy (6% Al, 1% Zn) showed low attenuation. In pure Mg, the transverse mode C_{dt} values increased over C_d by a factor from 2.4 to 4.1, while AZ61 Mg alloy gave approximately comparable attenuation between the two modes at 2 to 4 dB/m/MHz. No scattering contribution was visible. An early work on AZ31 Mg alloy with 3% Al [16] gave α_t (4.1 dB/m at 10 MHz) being 40% less than α . Both values were small, and when the diffraction correction is made, attenuation becomes nondetectable. Thus, our data is slightly higher. Low frequency damping data [42] listed η for pure Mg at 0.014–0.06 ($f = 60$ –400 Hz) or more than ten times the η or η_t values in Table 3. These η values were taken at strain amplitudes higher than 10^{-4} and activated large scale dislocation glide.

In pure Ni (grade 200), effects of cold work and magnetic field were significant. The effects were stronger for the transverse mode. In the annealed condition (Test N70), the C_{dt}/C_d ratio is 5, with C_{dt} reaching 300 dB/m/MHz. This dropped to about $\frac{1}{2}$, when two strong magnets were placed on the sides of the Ni sample (32 mm diameter). The magnets were F \times Nd-B type with the surface magnetic field of 5.6 kGauss (size: 25.4 mm diameter, 19 mm thick). C_d also decreased by 20% and further decreased to $\frac{1}{2}$ of the unmagnetized condition when one more magnet was applied. C_{dt} was unaffected by the additional magnetic field. In cold-worked Ni (Test N72), both C_{dt} and C_d were approximately 20 dB/m/MHz and were unaffected by magnetic fields. Such effects were

expected [44,45], but were insignificant in iron or steel. Large effects on the transverse attenuation of Ni were surprising. Reported attenuation values for Ni (grade A, equivalent to 200 grade) were C_d of 38.3 and C_{dt} of 120 dB/m/MHz [46]. These were 30 to 60% lower than Test N70. Since cold-work effects are strong, slight straining can cause such reduction.

In three single phase Ni alloys, Monel 400, Inconel 600 and 625, C_{dt} increased over C_d and their variations were large, ranging from 20 to 180 dB/m/MHz. Lower values of Inconel 625 alloy appear to come from cold work. Similar changes were found for Inconel 718 and 738 alloys, but hardening is presumably from precipitation hardening. Known heat treatment history is needed for further exploration. One single crystal Ni₃Al sample provided C_d and C_{dt} values and the latter was nearly twice larger, as in many of Ni-base alloy results. Using an Inconel 738 plate, directional anisotropy of C_d and C_{dt} was evaluated. Since C_d for the L orientation showed the frequency-squared dependence, direct comparison is difficult. However, the overall behavior appears to be identical to most other directional tests conducted. That is, the attenuation becomes higher in the order of L, T, and S orientation. This means that this plate underwent mechanical processing after casting. In some Al alloy bars, however, extrusion was apparently used and S orientation was similar to T orientation without showing the highest attenuation.

The final group includes two Ti alloys, Ti-6-4 and Ti-6-6-2 and tungsten (W). The C_d and C_{dt} values for Ti-6-4 and tungsten were comparable, while these for Ti-6-6-2 showed the usual factor of two increase for the transverse mode. Similar C_d and C_{dt} values were also found in seven other tests for Cu alloys (N44, N45, N64, N103), Ni (N72), and Inconel 738 (N109, N110). Tungsten is another metal beside Al with elastic isotropy. Its high hardness should suppress dislocation damping, but its attenuation values were comparable to Al alloys at 12 to 13 dB/m/MHz. In fact, C_{dt} values of Al alloys were often higher than W. This finding does support the dislocation bow-out mechanism for damping [13]. Reasons for comparable attenuation between the two vibration modes and the absence of hardness effect need further studies.

3.3. Attenuation Behavior of Organic Materials

Nine engineering polymers were evaluated for transverse attenuation and the results are summarized in Table 4 in the same format as before. Tests were conducted at 25 ± 2 °C. TDM-2 was used for all the samples, and TDM-1 was also used for PMMA, PVC, and PC. Only the average values for PMMA from Table 1 are listed in Table 4. The transverse attenuation of eight other polymers was higher than that of PMMA. Their C_{dt} values ranged from 717 to 1830 dB/m/MHz, or about 3 to 7 times higher. The averaged C_{dt}/C_d value was 3.1. All the transverse attenuation spectra showed the linear frequency dependence and scattering effect was absent. The transverse damping factor, η_t , did increase over the longitudinal damping factor, η , but η_t/η averaged to 1.53 or an increase of 53% since the starting average value of η was already high at 0.033. The average observed ratio of transverse and longitudinal damping factor of 1.62 agrees well with the same ratio of PMMA measured at lower frequencies (see Section 2). The transverse attenuation measurement used here can be used to extend low-frequency torsional methods for the study of transverse damping in polymers into the MHz range.

Table 4. Attenuation coefficients of longitudinal and transverse modes of organic materials.

Test No	Material	C_d	v	η	C_{dt}	v_t	η_t	C_{dt}/C_d	η_t/η	Thickness	Density	Notes
		$\text{dB/m}/\text{MHz}$	$\text{mm}/\mu\text{s}$		$\text{dB/m}/\text{MHz}^4$	$\text{mm}/\mu\text{s}$				mm	Mg/m^3	
O1	PMMA	91.4	2.40	8.00×10^{-3}	253	1.40	1.30×10^{-2}	2.78	1.62		0.95	TDM-1 Average
O2	PVC	239	2.33	1.91×10^{-2}	829	1.11	3.37×10^{-2}	3.47	1.65		1.40	
O2a	PVC				849	1.11	3.45×10^{-2}			8.6	1.40	TDM-1
O2b	PVC				728	1.11	2.96×10^{-2}			8.6/4.3	1.40	
O2c	PVC				909	1.11	3.70×10^{-2}			4.3	1.40	Average
O3	PC	638	2.25	5.26×10^{-2}	1780	0.98	6.40×10^{-2}	2.80	1.22		1.20	
O3a	PC				1750	0.97	6.22×10^{-2}			2.33	1.20	TDM-1
O3b	PC				1830	0.98	6.57×10^{-2}			4.7	1.20	
O3c	PC				1770	0.98	6.36×10^{-2}			2.33/4.7	1.20	
O5	Low density polyethylene (LDPE)	446	2.59	4.23×10^{-2}	1240	1.25	5.68×10^{-2}	2.78	1.34	24.2	0.91	TDM-1
O5a	Low density polyethylene (LDPE)	579	2.64	5.60×10^{-2}	1240	1.25	5.68×10^{-2}	2.14	1.01	24.2	0.91	
O10	High density polyethylene (HDPE)	222	2.51	2.04×10^{-2}	1010	1.17	4.33×10^{-2}	4.55	2.12	9.9	0.94	TDM-1
O6	Ultrahigh molecular weight PE	256	2.40	2.25×10^{-2}	990	1.33	4.82×10^{-2}	3.87	2.14	10.0	0.95	
O7	Polypropylene (PP)	452	2.61	4.32×10^{-2}	1260	1.38	6.37×10^{-2}	2.79	1.47	9.4	0.90	TDM-1
O7a	Polypropylene (PP)	465	2.61	4.45×10^{-2}	1260	1.38	6.37×10^{-2}	2.71	1.43	9.4	0.90	
O8	Nylon 6/6	269	2.67	2.63×10^{-2}	717	1.20	3.15×10^{-2}	2.67	1.20	27.3	1.14	TDM-1
O8a	Nylon 6/6	231	2.68	2.27×10^{-2}	717	1.20	3.15×10^{-2}	3.10	1.39	27.3	1.14	
O9	Epoxy	274	2.75	2.76×10^{-2}	1030	1.38	5.21×10^{-2}	3.76	1.89	9.1	1.39	TDM-1
	Average			3.27×10^{-2}			4.65×10^{-2}	3.12	1.54			

Figure 8 shows the attenuation spectra of PMMA (green curve for a TDM-1 result and purple for TDM-2), PVC (blue), and PC (red). Each has the least-square fit dotted line in the same color and R^2 values were 0.994, 0.997, 0.996, and 0.998, indicating good overall linearity.

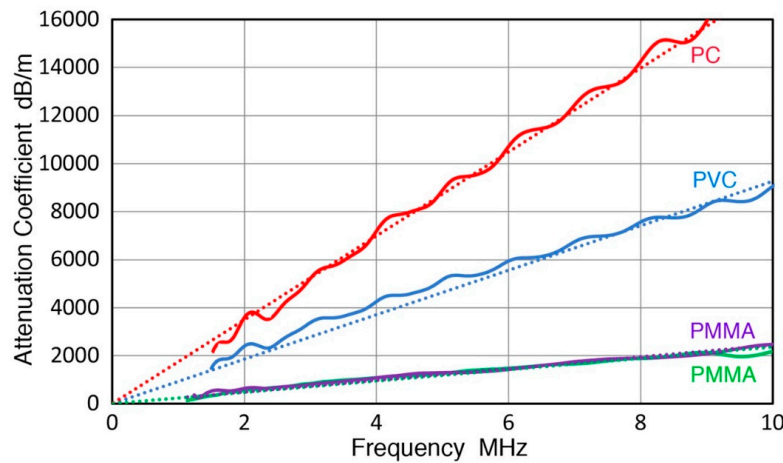


Figure 8. The transverse attenuation spectra of PMMA (green curve for TDM-1 and purple for TDM-2), PVC (blue), and PC (red). The least-square fits are shown in dotted lines of the same color.

When one attempts to correlate the C_d and C_{dt} values of polymers to the elastic moduli or sound velocities, general trends can be seen, except PMMA values always remain as outliers. The crystallinity, X_c , is another possible microstructural feature [47,48], but the attenuation values vary widely (by a factor of seven) among amorphous polymers of PMMA, PC, polypropylene (PP), and epoxy, for which $X_c = 0$. PMMA gives the lowest C_d or C_{dt} values and PC the highest. Semi-crystalline polymers of PVC ($X_c = 10\%$), Nylon 6/6 ($X_c = 40\%$), low-density polyethylene (LDPE; $X_c = 40\%$), high-density polyethylene (HDPE; $X_c = 63\%$), and UHMWPE ($X_c = 70\%$) showed relatively unchanged attenuation values. Here, X_c values were from [49–52]. Figure 9 shows the plots of C_d and C_{dt} vs. X_c . Fitting curves are shown, but clearly these are of no value. The above attempts offered no clue in regard to the factor(s) controlling C_d or C_{dt} values. A possible source of varying attenuation among amorphous and semi-crystalline polymers is the internal stresses from processing. It was noted earlier (in Section 2) that the external stress affected the attenuation in PMMA, shown by Saltiel et al. [38]. The cooling speed is a part of some polymer studies e.g., [47] and correlating it with attenuation and stressing may provide a needed key to understand the damping behavior of polymers. However, defining internal stresses carries its own problems since a reference state does not exist unlike its crystalline counterpart, as discussed by Alexander [53]. Even in the absence of a load, an amorphous solid always has internal stresses, which build up within the material as it solidifies. A new theory on amorphous solids was applied on sound attenuation of silica, but at THz frequencies [54,55]. Its applicability to MHz attenuation is unknown. For our purpose, macroscopic residual stress measurement methods [56,57] should work adequately.

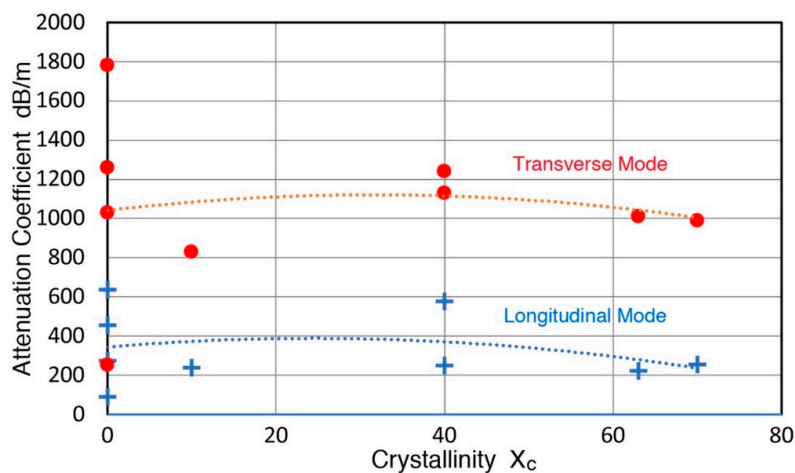


Figure 9. Longitudinal (blue) and transverse (red) attenuation coefficients vs. nominal crystallinity of polymer samples.

3.4. Attenuation Behavior of Fiber-Reinforced Plastics

Eight fiber-reinforced plastics (FRP) were evaluated for transverse attenuation and the results are summarized in Table 5 in a similar format as before, but using C_3 and C_{2t} coefficients in lieu of C_R and C_{Rt} . Sources of the FRP samples were described in [13], but the types of epoxy used for glass fiber-reinforced plastics (GRP) and Kevlar fiber-reinforced plastics (KFRP) were unavailable. Cross-plyed (XP) GRP and KFRP used woven rovings. Matrix resin types of AS4, G50, and T700 carbon fiber reinforced plastics (CFRP) were Hexcel 3501-6, Hexcel F584, and Toray 2510, respectively. G50 XP-CFRP had a layup of $(0^\circ_2, 90^\circ_2)_{4s}$. Eighteen transverse and two additional longitudinal tests were conducted at 25 ± 2 °C. Except for two tests, the transverse attenuation coefficients, C_{dt} , were more than 1.5 times higher than the corresponding C_d values, with the average C_{dt}/C_d ratio of 4.45. Even when waves move along the orientation parallel to the fibers, C_{dt} values exceeded 300 dB/m/MHz, well above that of PMMA. This reflects low wave velocities parallel to fibers (1.75–2.15 mm/ μ s), which are similar to the transverse or matrix wave velocities (1.3–1.9 mm/ μ s). That is, the transverse wave propagation is controlled by the matrix primarily. When waves propagated normal to parallel fibers (Tests R4 and R16), the cubic frequency dependences were observed for the longitudinal attenuation (see for example, Figure 10, red curve), but the f^3 contribution vanished and only linear frequency spectra were observed (see Figure 11, dark red curve). One case with non-zero C_R term (Test R26) also lost the scattering contribution. Thus, the linear frequency spectra were predominantly observed for the transverse mode. Apparently, parallel fibers have a lower scattering cross section in the transverse wave mode. However, the wave velocity was always higher by 10% when the polarization direction coincided with the fiber orientation, implying the existence of transverse wave \times fiber interaction.

Table 5. Attenuation coefficients of longitudinal and transverse modes of fiber-reinforced plastics.

Test.	Material	C _d	C ₃	v	η	C _{dt}	C _{2t}	v _t	η _t	C _{dt} /C _d	η _t /η	Thickness	Density	Notes
No		dB/m /MHz	dB/m /MHz ³	mm /μs		dB/m /MHz	dB/m /MHz ²	mm /μs				mm	Mg/m ³	
R1	GRP rod //F	74.6		4.96	3.00 × 10 ⁻²	478		1.71	3.00 × 10 ⁻²	6.41	2.21	33.5	1.97	
R4	GRP rod SN	173	5.946	3.07	5.72 × 10 ⁻²	952		1.64	5.72 × 10 ⁻²	5.50	2.94	6.3	1.97	pol = ⊥F
R4a	GRP rod SN	173	5.946	3.07	6.09 × 10 ⁻²	944		1.76	6.09 × 10 ⁻²	5.46	3.13	6.3	1.97	pol = //F
R5	GRP //F	121		5.06	4.29 × 10 ⁻²	650		1.80	4.29 × 10 ⁻²	5.37	1.91	7.0	2.07	Pultruded rod
R13	GRP XP //F	202		4.15	1.27 × 10 ⁻¹	1740		1.99	1.27 × 10 ⁻¹	8.61	4.13	7.0	1.81	
R14	GRP XP SN	441		2.84	1.83 × 10 ⁻¹	3030		1.65	1.83 × 10 ⁻¹	6.87	3.99	2.2	1.81	pol = //F
R15	CFRP AS4 UD //F	91.0		9.32								36.6	1.53	
R35	CFRP AS4 UD //F	65.2	(0.0372: n = 4)	9.20	3.15 × 10 ⁻²	326	74.4	2.15	3.15 × 10 ⁻²	3.58	1.02	5.4	1.53	
R35a	CFRP AS4 UD //F	65.2	(0.0372: n = 4)	9.20	1.10 × 10 ⁻²	0	140	2.15	1.10 × 10 ⁻²	2.15	0.50	5.4	1.53	
R16	CFRP AS4 ⊥F	247	4.938	3.16	4.43 × 10 ⁻²	579		2.09	4.43 × 10 ⁻²	2.34	1.55	24.3	1.53	pol = //F
R16a	CFRP AS4 ⊥F	247	4.938	3.16	3.42 × 10 ⁻²	583		1.60	3.42 × 10 ⁻²	2.36	1.20	24.3	1.53	pol = ⊥F
R18	CFRP G50 UD //F	110		11.30	4.99 × 10 ⁻²	667		2.04	4.99 × 10 ⁻²	6.06	1.09	13.3	1.58	
R22	CFRP G50 UD SN	148		2.79	6.71 × 10 ⁻²	995		1.84	6.71 × 10 ⁻²	6.72	4.43	28.9	1.58	pol = //F
R22a	CFRP G50 UD SN	148		2.79	5.01 × 10 ⁻²	1050		1.30	5.01 × 10 ⁻²	7.10	3.31	28.9	1.58	pol = ⊥F
R36	CFRP G50 XP SN	213		2.68	4.21 × 10 ⁻²	709		1.62	4.21 × 10 ⁻²	3.33	2.01	4.7	1.58	
R26	CFRP T700 UD //F	68.6	(0.0316: n = 4)	9.19	3.77 × 10 ⁻²	527		1.95	3.77 × 10 ⁻²	7.68	1.63	23.7	1.48	
R28	CFRP T700 UD SN	1730		2.66	9.70 × 10 ⁻²	1400		1.89	9.70 × 10 ⁻²	0.81	0.57	15.5	1.48	pol = //F
R28a	CFRP T700 UD SN	1730		2.66	1.12 × 10 ⁻²	1860		1.64	1.12 × 10 ⁻¹	1.07	0.66	3.5	1.48	pol = ⊥F
R34a	KFRP SN	1090		2.72	7.88 × 10 ⁻²	1630		1.32	7.88 × 10 ⁻²	1.50	0.73	9.2	1.34	
R34b	KFRP SN	1090		2.72	8.29 × 10 ⁻²	1700		1.33	8.29 × 10 ⁻²	1.56	0.77	4.41	1.34	
	Average				6.52 × 10 ⁻²				6.52 × 10 ⁻²	4.45	1.99			

//F: Parallel to fibers; SN: Normal to plate surface; ⊥F: Normal to fibers in the transverse direction; pol: The direction of polarization of transverse waves.

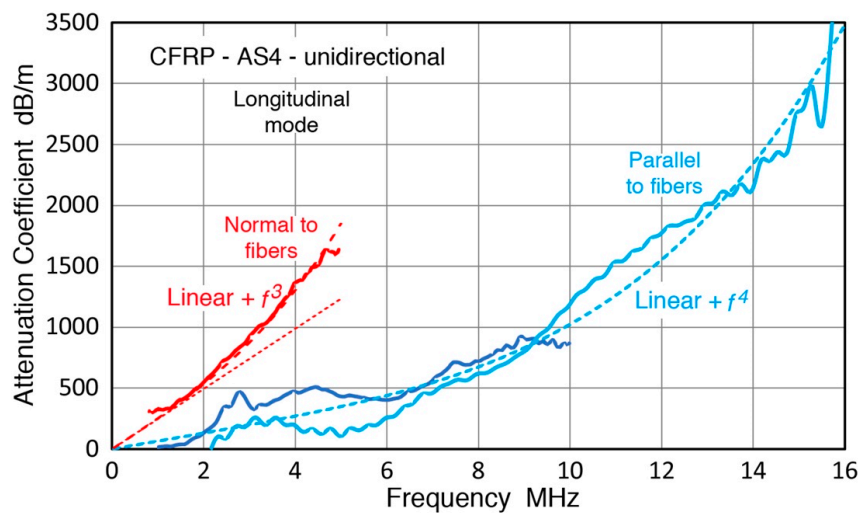


Figure 10. The longitudinal attenuation spectra of a unidirectional (UD) carbon fiber reinforced plastic (CFRP) with AS4 fibers. Wave direction was parallel to fibers (blue curves, fitted to Mason-McSkimin or to linear + f^4 relation) or normal to fibers (red curve, fitted to linear + f^3 relation). Fitted curves in dashed plots (a red dotted line is for linear fit).

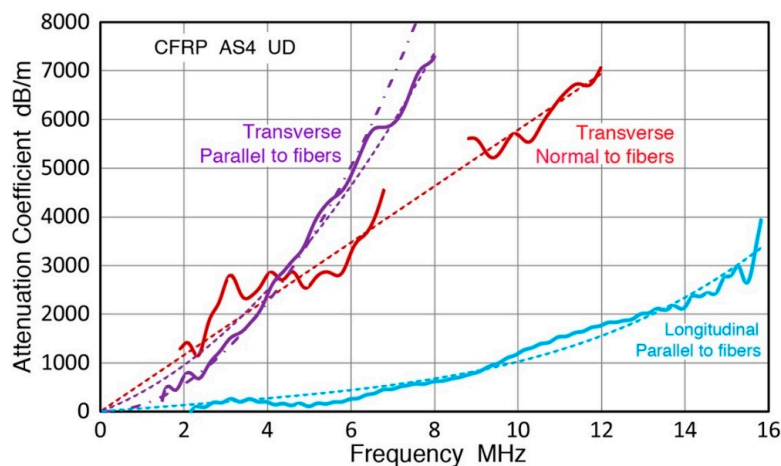


Figure 11. The transverse attenuation spectra of AS4 UD-CFRP. Purple curve: Transverse attenuation parallel to fibers. A linear + f^2 fit (dashed curve) and a f^2 fit (dash-dotted) are also plotted. Dark red: Transverse attenuation normal to fibers, with the polarization parallel to fibers. A linear fit is in the dotted line. A longitudinal attenuation spectrum from Figure 10 is shown in light blue with a Mason-McSkimin fit (dashed curve).

One repeat test for a carbon fiber reinforced plastic (CFRP) with unidirectional (UD) AS-4 fibers (Test R15a) showed a linear attenuation spectrum plus a C_R (the 4th power of frequency) contribution in the orientation parallel to the fibers. This is one of the additional longitudinal tests and results are shown in Figure 10. In the previous work, the test was limited to 10 MHz and the C_R part was not recognized, as shown in a blue curve. A new test extended the frequency limit to 16 MHz (by using Olympus V111 as a transmitter in place of an older V1030, though both are 10 MHz transducers). This spectrum (light blue curve) can be fitted to the Mason-McSkimin relation with a linear part plus f^4 part. The fitted spectrum is plotted in a dashed curve. Additionally shown in Figure 10 for a comparison, is the longitudinal attenuation for the surface normal orientation (red curve), as noted above. Figure 11 gives the transverse attenuation spectra along the fiber direction (purple curve, Test R15a). The polarization was along the fibers. This is to be compared to the light blue curve, replotted from Figure 10, representing the Mason-McSkimin spectrum for the same orientation. The sample for the

transverse attenuation was cut from a longer sample used for the previous longitudinal test (Test R15). The transverse attenuation increased rapidly with increasing frequency and became more than ten times higher than the longitudinal value at 5 MHz and the difference expanded further as f increased. This attenuation curve has two possible fitting functions (shown as in purple dash and dash-dotted curves). These are:

$$\alpha_t = 326 f + 74.4 f^2 \tag{13}$$

and

$$\alpha_t = 140 f^2 \tag{14}$$

However, no theoretical basis exists for the use of frequency-squared relations. Equation (14) gives $R^2 = 0.998$ in a least-square fitting, so a good fit does exist. The dark red curve is a plot of the transverse attenuation when waves enter a CFRP sample in the direction normal to fibers. This is to be compared to the red curve in Figure 10, which had a cubic spectral component of the Biwa relation. While the dark red curve has larger fluctuation, a linear fit best describes its behavior. The attenuation levels were similar to those of the purple curve along the fibers below 5 MHz, but rose more slowly at higher frequencies. The transverse attenuation showed usual behavior initially with less attenuation in the propagation direction parallel to fibers. Due to the cubic term, however, the attenuation along the fibers overtook transverse attenuation moving normal to fibers above 5 MHz.

The absence of the cubic dependence for the propagation normal to fibers (dark red curve), predicted by the Biwa theory [58], was unexpected, but a high matrix attenuation may have hidden the scattering effects. The presence of frequency-squared spectra in the case of wave propagating parallel to fibers and weaker scattering effects are the issues needing further study.

All the UD composite samples are transversely isotropic (and woven cross-ply composites may be approximated the same for the surface normal orientation), wave velocity, and mass density data was used to estimate the elastic compliance values of C_{11} , C_{33} , C_{12} , C_{44} , and C_{66} , using relationships given by Prosser [59]. Results are tabulated in Table 6. The corresponding damping factors are designated as η_{11} , η_{33} , η_{44} , and η_{66} and also listed in Table 6, with the cross-plyed (XP) data separated at the bottom as these are less reliable due to the approximation used. Density, fiber mass % values, and notes on epoxy are added from the previous report, except for the XP-glass fiber reinforced plastic (GRP) [60]. Epoxy and PMMA data from Table 4 was also converted and added to the table for comparison.

Table 6. Elastic moduli and damping factors of fiber-reinforced plastics.

	C_{11}	C_{33}	C_{12}	C_{44}	C_{66}	η_{11}	η_{33}	η_{44}	η_{66}	Density	Fiber	Notes
	GPa	GPa	GPa	GPa	GPa					Mg/m ³	Content %	
GRP rod	18.57	48.47	7.97	6.10	5.76	0.019	0.014	0.061	0.030	1.97	56.5	
GRP pultruded		53.00			6.71		0.022		0.043	2.07	61.5	
CFRP AS4 UD	15.28	132.9	7.44	6.68	7.07	0.029	0.031	0.044	0.032	1.53	50.0	Hexcel 3501-6
CFRP G50 UD	12.30	201.8	6.96	5.35	6.58	0.015	0.046	0.067	0.050	1.58	60.0	Hexcel F584
CFRP T700 UD	10.47	125.0	2.51	5.29	5.63	0.169	0.023	0.097	0.038	1.48	41.0	Toray 2510
GRP XP	14.60	31.17		4.93	7.17	0.046	0.031	0.183	0.127	1.81	38.0	woven
G50 XP	11.35			4.15		0.021		0.042		1.58	60.0	Hexcel F584
KFRP	9.91			2.33		0.108		0.079		1.32	32.0	Woven
Epoxy	10.51			2.65		0.028	0.028	0.052	0.052	1.39		
PMMA	5.47			1.86		0.008	0.008	0.013	0.013	0.95		

The 3-direction is parallel to fibers.

Damping factor, η_{33} , is for the longitudinal wave propagation parallel to the fibers. It is mostly below that of epoxy (not of the types used for composite matrices). As the epoxy volume is reduced by fibers, even lower η_{33} should be expected from theory (e.g., [17,18,58]). However, high modulus fibers raise the sound velocity, partly contributing to high η_{33} values. For the transverse wave propagation parallel to the fibers, η_{66} describes the damping behavior. These are higher than η_{33} and all η_{66} values exceeded 60% of epoxy value. Another transverse damping factor, η_{66} , mostly was higher than epoxy as the shearing motion is parallel to fibers offering no resistance. Among the UD composites, T700 CFRP produced the highest values of η_{11} and η_{44} . The matrix was from a toughed resin from the Toray 2501

prepreg system and appeared to result in strong damping. Relatively high η_{ij} values of G50 CFRP were surprising as its matrix of F584 was a standard aerospace grade. In addition, this CFRP has the most metallic sounds when hit with a metal rod. Woven FRP produced high damping factors as fiber volumes were low and continuous resin layers were present.

Damping factors of nine GRP and CFRP samples from six studies were compiled in [12]. All of them used the double through-transmission method [24,30–35]. The ranges of damping factors are generally comparable to those in Table 6. However, the details of these composite samples were unavailable. Without the knowledge of fiber types, volumes, as well as matrix resin types, further comparison adds little.

3.5. Attenuation Behavior of Inorganic Materials

Twenty-four inorganic materials were evaluated for transverse attenuation and the results are summarized in Table 7 in a similar format as Table 3. Most of them were ceramics and rocks, but silicon cannot be categorized as either. Thirty-five test results are listed as multiple tests were done for some materials. Nine materials were added to the samples used in [13]. These are Pyrex glass (Tests C41, C42), soda-lime glass (Test C43), tempered soda-lime glass (Test C44), fused silica (Test C45), sapphire single crystal (Test C46), calcite (a duplicate sample; Test C47), quartz single crystal (Test C48), silicon single crystal (Test C49), and rock salt (Test C50). Many large or highly attenuating samples from the previous work [13] were not tested since these require a pair of lower frequency transducers. Machine shop access was also unavailable to prepare thinner samples.

Transverse attenuation showed mostly the linear frequency dependence except for four cases. The C_{dt} values ranged from non-detectable for fused silica, which also had $C_d = 0$, to 876 dB/m/MHz for granite (Santa Cecilia). Only three cases showed the Rayleigh scattering term, one of which can be fitted to the frequency-squared spectrum as well. Marble again showed the frequency-squared spectrum, attributed to the multiple scattering mechanism [13]. The Rayleigh term was large for SiC, which showed only the linear spectrum for the longitudinal mode. In contrast, mortar had a large C_R value for the longitudinal spectrum, but it disappeared for the transverse mode. Such opposite behaviors require further studies. The levels of damping factors were generally high, the highest shown by granite at 0.22. The average of η_t was 0.038, which is 15% higher than the corresponding average for the polymers (cf. Table 4). The average of C_{dt}/C_d ratio was 1.27, whereas the average of η_t/η ratios was 0.72. Nearly half of the samples exhibited lower transverse attenuation than longitudinal attenuation; i.e., $C_d > C_{dt}$. Most amorphous materials belonged to this group. Four more showed comparable C_d and C_{dt} values (within $\pm 20\%$). Only ten had clearly higher C_{dt} values than C_d values. This group included mortar, PZT-5, soda-lime glass, ceramic tile, SiC, Macor glass-ceramic, marble (Carrara), quartz single crystal, Si single crystal, and rock salt. Note that the high C_{dt} group mostly has crystalline ceramics (plus Si), but soda-lime glass is an exception.

A group of widely used engineering ceramics that includes porcelain, alumina, transparent alumina (Lucalox), and sapphire single crystal showed the unexpected characteristic of less than unity C_{dt}/C_d ratios. This ratio varied from 0.31 to 0.59, averaging at 0.48. This trend is shared by BK7 and Pyrex glasses and tempered soda-lime glass, but untampered (slow-cooled) soda-lime glass has an opposite behavior with C_{dt}/C_d of 1.86. These materials have both covalent and ionic bonding, but produced C_{dt}/C_d ratios above and below unity. A strongly ionic solid of rock salt and covalently bonded Si have high C_{dt}/C_d ratios of 4.32 and 5.84, making it impossible to correlate the observed attenuation behavior to the atomic bonding characters. It was hoped before these tests that the atomic bonding characters may explain the relative levels of longitudinal and transverse attenuation. The varied attenuation behaviors observed require a different approach.

Table 7. Attenuation coefficients of longitudinal and transverse modes of ceramics and rocks.

Test.	Material	C _d	C _R	v	η	C _{dt}	C _{Rt}	v _t	η _t	C _d /C _d	η _t /η	Thickness	Density	Notes
No.		dB/m /MHz	dB/m /MHz ⁴	mm /μs		dB/m /MHz	dB/m /MHz ⁴	mm /μs				mm	Mg/m ³	
C1	Mortar	252.0	6.20 × 10	3.71	3.43 × 10 ⁻²	423		2.18	3.38 × 10 ⁻²	1.68	0.99	50.7	2.00	
C4	WC	41.9		6.75	1.04 × 10 ⁻²							31.0	14.51	
C4a	WC	46.8		6.76	1.16 × 10 ⁻²	51.9		4.07	7.74 × 10 ⁻²	1.17	0.67	31.0	14.51	
C7	PZT-5A	242.0		4.38	3.88 × 10 ⁻²	509		1.72	3.21 × 10 ⁻²	2.10	0.83	5.3	7.78	
C8	BaTiO ₃	121.0		5.91	2.62 × 10 ⁻²							4.2	5.70	
C8a	BaTiO ₃	105.0		6.29	2.42 × 10 ⁻²	89.3		3.60	1.18 × 10 ⁻²	1.08	0.49	4.2	5.70	
C9	BK7 glass	5.0		5.80	1.06 × 10 ⁻³	4.7		3.46	5.96 × 10 ⁻⁴	0.94	0.56	100.0	2.51	
C10	BK7 glass	6.3		5.80	1.34 × 10 ⁻³							50/100	2.51	TDM-1
C10a	BK7 glass					3.4		3.46	4.31 × 10 ⁻⁴	0.60	0.36	3.3/100	2.51	TDM-1
C10b	BK7 glass					4.5		3.46	5.71 × 10 ⁻⁴	0.80	0.48	100.0	2.51	
C10c	BK7 glass					4.3		3.46	5.45 × 10 ⁻⁴	0.76	0.45	16/100	2.51	TDM-1
C41	Pyrex glass	10.5		5.52	2.12 × 10 ⁻³	4.9		3.41	6.12 × 10 ⁻⁴	0.46	0.29	76.0	2.23	
C42	Pyrex glass	10.7		5.52	2.16 × 10 ⁻³	2.1		3.41	2.62 × 10 ⁻⁴	0.20	0.12	16/76	2.23	TDM-1
C42a	Pyrex glass					1.4		3.41	1.75 × 10 ⁻⁴	0.13	0.00	3.3/76	2.23	TDM-1
C43	Soda-lime (S-L) glass	8.7		5.86	1.87 × 10 ⁻³	16.2		3.50	2.08 × 10 ⁻³	1.86	1.11	5.6	2.48	
C44	S-L glass, tempered	12.3		5.83	2.63 × 10 ⁻³	8.8		3.47	1.12 × 10 ⁻³	0.72	0.43	10.2	2.52	
C45	Fused silica	ND		5.87		ND		3.71				3.0/45	2.20	TDM-1
C21	Clay ceramic (tile)	193.0	5.07 × 10 ⁻¹	3.93	2.78 × 10 ⁻²	239	7.84 × 10 ⁻¹	2.47	2.16 × 10 ⁻²	1.24	0.78	6.9	1.97	
C21a	Clay ceramic (tile)					0	(78.57: n = 2)	2.48	7.14 × 10 ⁻³			6.9	1.97	
C24	Porcelain	167.0		5.75	3.52 × 10 ⁻²	85.8		4.15	1.30 × 10 ⁻²	0.51	0.37	2.1	2.63	
C24a	Porcelain	173.0		7.14	4.53 × 10 ⁻²	98		4.15	1.49 × 10 ⁻²	0.57	0.33	2.0	2.63	
C25	Sintered Alumina	196.0		9.43	8.32 × 10 ⁻²	116		5.47	5.93 × 10 ⁻²	0.76	0.41	3.3	3.42	
C26	Transparent alumina	336.0		10.70	1.32 × 10 ⁻¹	136		6.19	3.08 × 10 ⁻²	0.40	0.23	3.0	3.90	
C46	Sapphire SX	106.0		10.93	4.33 × 10 ⁻²	32.9		6.78	8.17 × 10 ⁻³	0.31	0.19	3.1	3.98	R-cut
C27	Bonded SiC	392.0		5.79	8.32 × 10 ⁻²	473	1.40 × 10	3.36	5.93 × 10 ⁻²	1.21	0.71	9.3	2.32	
C29	Macor	3.6		5.30	6.91 × 10 ⁻⁴	8.3	8.09 × 10 ⁻⁴	3.10	9.43 × 10 ⁻⁴	2.33	1.36	36.5	2.52	
C33	Granite (Santa Cecilia)	1129.0		5.22	2.16 × 10 ⁻¹							30.0	2.74	
C33a	Granite (Santa Cecilia)	1150.0		5.24	2.21 × 10 ⁻¹	867		2.82	8.96 × 10 ⁻²	0.76	0.41	30.0	2.74	
C35	Marble (Carrara)	0.0	(29.7: n = 2)	6.26	[6.81 × 10 ⁻³]		(57.3: n = 2)	3.34	7.01 × 10 ⁻³	1.93	1.03	29.0	2.83	
C38	Fluorite <111>	43.4		6.39	1.02 × 10 ⁻²	45.1		3.98	6.58 × 10 ⁻³	1.04	0.65	28.8	3.13*	
C39	Calcite [001][110]	58.8		7.25	1.56 × 10 ⁻²	40.9		2.72	4.08 × 10 ⁻³	0.70	0.26	22.1	2.72	yellow
C47	Calcite [001][110]	52.4	1.17 × 10 ⁻²	7.14	1.37 × 10 ⁻²	28.3		2.71	2.81 × 10 ⁻³	0.54	0.20	8.5	2.71	clear
C40	ADP H ₆ NO ₄ P <100>	0.0		6.17		2.38		2.20	1.92 × 10 ⁻⁴			73.0	1.8*	pol = <001>
C40a	ADP H ₆ NO ₄ P <100>					3.74		3.74	5.13 × 10 ⁻⁴			73.0	1.8*	pol = <010>
C48	Quartz SX SiO ₂ X	19.1		5.71	4.00 × 10 ⁻³	47.2		3.28	5.67 × 10 ⁻³	2.47	1.42	23.4	2.56	pol = Z
C49	Si SX	2.7		9.22	9.09 × 10 ⁻⁴	15.7		5.10	2.93 × 10 ⁻³	5.84	3.23	29.7	2.33	
C50	Rock salt	50.0	1.82 × 10 ⁻²	4.55	8.34 × 10 ⁻³	216		2.69	2.13 × 10 ⁻²	4.32	2.55	51.0	2.18	
	Average				3.86 × 10 ⁻²				1.19 × 10 ⁻²	1.26	0.70			

SX: Single crystal (fluorite, calcite, and ADP are also SX); pol: Polarization direction; <ijk> for ADP: Apparent growth orientations are used, since the Miller indices are complex.

4. Discussion

Ultrasonic attenuation coefficients for the transverse mode were measured and tabulated in Section 3 for 223 test samples. Their corresponding longitudinal attenuation coefficients were also given. The frequency dependence of the attenuation coefficients followed four patterns, linear, Mason-McSkimin (linear + f^4), linear + f^2 (or f^2), and linear + f^3 (or f^3). The distributions of attenuation spectra among the four patterns are summarized in Table 8 in the first five columns. Values shown are transverse test counts for each pattern separated into five material groups. Moreover, given in the parentheses are longitudinal test counts from the previous study [13]. Total test counts of the tabulated were 222 (fused silica test was omitted due to non-detection) and 348 for the transverse and longitudinal modes.

The distribution of spectral patterns of transverse attenuation were generally similar to that of longitudinal attenuation; 65% of the transverse tests exhibited the linear frequency dependence (vs. 67.5% for longitudinal). For the Mason-McSkimin relation with Rayleigh scattering contribution, these percentages were 28 and 22%, respectively. These distributions indicate that the linear damping component is dominant in the majority of the attenuation spectra in both modes of wave propagation. The percentages of two power-law distributions, f^2 or f^3 , were reduced in the transverse mode.

The next two columns give the range of the linear coefficient, C_{dt} . On the low side, C_{dt} is zero when a power-law component describes the attenuation spectrum. For these cases, the next low value is listed (in parentheses). Metal groups showed lower maximum C_{dt} values and polymers and FRP groups the highest, over 1800 dB/m/MHz.

When attenuation coefficients of two modes of wave propagation are compared, most of the polymers and FRP groups showed higher C_{dt} than C_d values. In contrast, the ferrous and ceramics and rocks group gave more even distributions of C_{dt}/C_d ratios. These are shown in columns 8 to 10. C_{dt}/C_d ratios were separated into three: $C_{dt}/C_d \geq 1.5$, $1.5 > C_{dt}/C_d \geq 0.67$, and $0.67 > C_{dt}/C_d$. About 2/3 of the non-ferrous group had high C_{dt}/C_d ratios, but the rest were of comparable or lower C_{dt} than C_t . Over all the test results, 61% showed C_{dt}/C_d ratio high than 1.5, indicating that transverse attenuation coefficients are higher than longitudinal ones in the majority of materials. However, the opposite or comparable cases are not negligible, especially in the ferrous group or in the ceramics and rocks group.

The final two columns present the average values of damping factors, η and η_t . These were calculated for each group. Three groups of FRP, polymers, and ceramics and rocks have high η and η_t values above 0.012. Recall that PMMA had η and η_t values of 0.008 and 0.013. That is, these three groups showed on average comparable or higher damping factors than one of the representative viscoelastic solids. Both metal groups had lower damping factors, but the average η values were only 20% lower than that of PMMA and η_t values 45 and 70% down. The only one that is clearly outside of the viscoelastic solid category is fused silica. Its attenuation was not detected with the measurement sensitivity of the methods used in this work. Thus, most test samples used in this study may be designated to be viscoelastic solids. For such solids, Knopoff [1] derived a connecting equation between the viscosity term of the Kelvin-Voigt solid and $Q^{-1} = \eta = 2\pi f \eta_{KV}/E'$, as noted in Section 1. However, the use of damping factors as the sole criterion for viscoelastic designation appears to require further verification regarding the applicability of the Knopoff equation to MHz frequencies. It is also necessary to find physical mechanisms of damping, especially in strong solids, such as Inconel 600, sapphire, and granite. These have damping factors (η) 2.5-, 5.4-, and 27-times higher than that of PMMA. While the dislocation bow-out mechanism [13] can possibly account for the case of Inconel 600, it is particularly difficult for sapphire with no grain boundaries and extremely high hardness (with a measured Vickers HN of 1760). Further studies are warranted.

Table 8. General characteristics of attenuation parameters according to material groups.

Material Group	C _{dt} Only	C _{dt} + C _R or C _R	C _{dt} + C ₂ or C ₂	C _{dt} + C ₃	C _{dt} – Low dB/m/MHz	C _{dt} – High dB/m/MHz	C _{dt} /C _d ≥ 1.5	1.5 > C _{dt} /C _d ≥ 0.67	0.67 > C _{dt} /C _d	η	η _t
Ferrous	23 (73)	28 (35)	2 (13)	0 (0)	0 (1.4)	164	17	21	15	6.69 × 10 ⁻³	3.97 × 10 ⁻³
Non-ferrous	41 (59)	31 (29)	7 (11)	2 (0)	0 (4.0)	341	54	16	11	6.52 × 10 ⁻³	7.28 × 10 ⁻³
Polymers	37 (48)	0 (2)	0 (4)	0 (0)	211	1830	37	0	0	3.27 × 10 ⁻²	4.65 × 10 ⁻²
Fiber-reinforced plastics	17 (25)	0 (1)	2 (0)	0 (8)	0 (326)	1860	17	2	0	4.79 × 10 ⁻²	6.52 × 10 ⁻²
Ceramics and rocks	27 (30)	3 (8)	2 (2)	0 (0)	0 (1.4)	867	10	11	11	3.86 × 10 ⁻²	1.19 × 10 ⁻²
Percent of total tests	65.3 (67.5)	27.9 (21.6)	5.9 (8.6)	0.9 (2.3)			60.8	22.5	16.7		

Values in parentheses in columns 2 to 5 are for the longitudinal mode. Those in column 6 refer to the second lowest C_{dt}. Tested sample counts for ceramics and rocks excluded fused silica since no attenuation was detected.

Atomic and molecular origins of low frequency damping in PMMA were listed in [61] and come from the molecular rotation of different parts of monomers (known as α , β , γ , and δ relaxations), backbone chain bending, and side \times chain tangling. Intermolecular vibration and density variation are other sources of energy loss [53,54]. Molecular dynamics (MD) simulations on PMMA [62] successfully constructed an amorphous PMMA model and obtained the density, elastic modulus, and thermal expansion coefficient, but the damping part remains unreported. Additional works on this subject were collected [63], but none dealt with the damping simulation. Other MD works deduced stress-strain relations of PC, PE, and polystyrene and their methods can possibly determine the hysteresis behavior under lower cyclic stressing [64,65]. Fang et al. [64] emphasized important roles of shear stresses in driving structural changes in glassy polymers. This appears to contribute to substantially higher transverse attenuation found in all the polymer samples tested in this study. In addition to the MD studies, a different approach of shear transformation zone (STZ) theory [66,67] can account for the shear deformation of amorphous silicon (obtained by a model calculation [68]). The STZ theory clearly showed a hysteresis effect at a near-yield stress. This behavior is likely to remain at low stresses. If so, the STZ theory in combination with the amorphous PMMA model [62] can be extended to common polymers, accounting for high C_{dt}/C_d ratios observed. Shear stress effects may also be connected to soda-lime glass damping as it alone showed a high C_{dt}/C_d ratio (1.86) together with the highest C_{dt} value among silicate glasses, while other silicate glasses had lower C_{dt}/C_d ratios (0.48 on average), as discussed in Section 3.5. It has been well known [69] that sodium and other cations can move under stress, contributing to vibration damping. Tempered soda-lime glass (Test C44) produced a reversal, reducing $C_{dt}/C_d = 0.72$. As the stress level in a tempered glass is expected to be 40–50 MPa at most [69], relatively low stresses can shift the positions of cations, changing the attenuation responses. Lower C_d and C_{dt} values in Pyrex and BK7 are attributed to lower alkali ion contents.

In many steels, C_{dt}/C_d ratios were lower than 1.5 and their average was 1.19. This observed similarity of C_d and C_{dt} values can be a consequence of the dislocation bow-out mechanism, proposed in [13]. A recent MD study of dislocation motion in bcc iron [70] predicted that an edge dislocation can move at 8.5 m/s/MPa. If this factor holds at kPa levels, dislocation damping can explain the observed levels of attenuation of both longitudinal and transverse modes. A screw dislocation was immobile, however.

A possible key to elucidate material parameters that control the C_{dt}/C_d ratios is Poisson's ratio, as Greaves et al. [71,72] showed many links between this non-dimensional elastic constant and the atomic and molecular bonding of solids. Figure 12 gives a plot of C_{dt}/C_d value vs. Poisson's ratio of 149 samples examined. The C_{dt}/C_d values are from Tables 1–7 and Poisson's ratios are from Tables A1–A3 in the Appendix A. Nearly a half of the samples had $C_{dt}/C_d < 1.5$ over the range of Poisson's ratio, ν , of 0.17 to 0.35. Most ceramics and rocks, 19 of 25 samples, and 2/3 of iron and steels showed C_{dt}/C_d lower than 1.5. These are mainly distributed in the range of ν between 0.2 and 0.3. On \times third of non-ferrous alloys also exhibited low C_{dt}/C_d values, but their ν range was higher from 0.28 to 0.35, reflecting their higher stiffness due to their closed-packed structures. All the polymers had high C_{dt}/C_d values above 2.5. The observed distribution of lower C_{dt}/C_d values in the range of ν , centering at about 0.27 may suggest a relation with the Cauchy solids with $\nu = 0.25$. These were based on the centric force hypothesis, which allows ready translational displacements [72]. Yet, this is contradicted by the observation of a high value of $C_{dt}/C_d = 4.3$ for rock salt (or NaCl), of which bonding is strongly ionic and non-directional. It is difficult to link the primary atomic bonding to MHz-range viscous vibrations of atoms and molecules, since atomic motions occur at THz frequencies. In amorphous solids, molecular rearrangements appear to supply the energy loss, while slow dislocation movements are likely to be the main cause of viscous damping in crystals. In annealed isotropic metals, for example, Al 6061 and tungsten showed similar attenuation coefficients even though the latter had 4-times higher hardness (cf. Table 3). However, hard solids present difficult issues as dislocations must overcome stronger barriers. For example, a hard crystal, such as sapphire (VHN = 1760), showed about 10-times C_{dt} value of soft ADP (VHN = 80). Many damping and internal friction mechanisms have been discussed

over time [73–75], but new ones are needed to understand various attenuation characteristics revealed in the present study. In this context, Gilman’s mechanism of bond bending for dislocation motion in covalent solids can be introduced to provide dislocation damping in hard solids [76]. However, even this bond bending scheme may be inadequate for the case of sapphire.

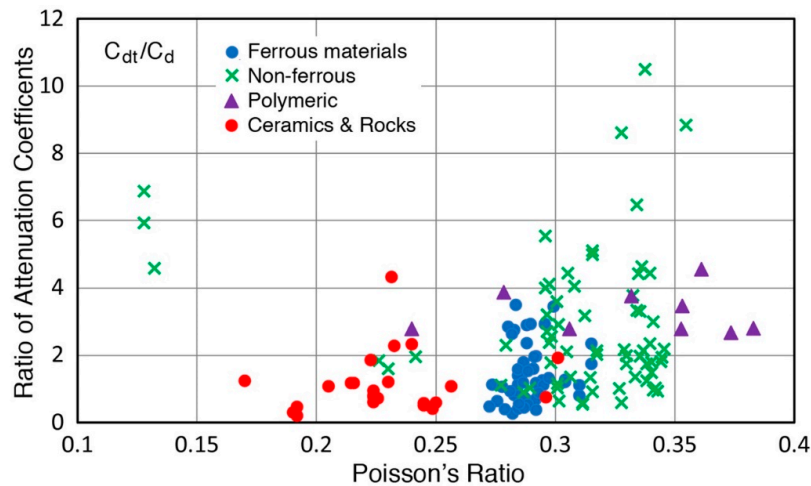


Figure 12. C_{dt}/C_d values vs. Poisson’s ratio of tested samples, grouped into four types, ferrous, non-ferrous, polymers, and ceramics and rocks. Note that the fraction of high C_{dt}/C_d is lower than in Table 8 because power-law fits were omitted for this data set.

The most significant result of the present inquiries along with [13] into the ultrasonic attenuation of solids was the presence of the damping effect, as reflected in the linearly dependent frequency spectra of attenuation coefficients. The cause of this effect has not been identified except in amorphous solids, as in polymers and silicate glasses. Theoretical approaches discussed above seem to provide rational explanation [53,61–68]. For metallic materials, the most plausible mechanism was provided in [13] relying on cyclic dislocation bow-out under imposed ultrasonic vibration. When the bonding becomes stronger in ionic and covalent solids, the dislocation bow-out is likely to be inadequate as the Peierls-Nabarro barriers become high. Kink motion as in bcc iron [70] may be a possible approach by using the MD calculation.

5. Summary

- (1) Methods of ultrasonic attenuation measurement for the transverse waves were implemented and verified using PMMA samples. These were transmission difference methods, similar to those used previously for the longitudinal waves [13].
- (2) A total of 223 transverse attenuation measurements were completed together with 50 additional longitudinal attenuation measurements. The frequency dependence of the attenuation coefficients followed four patterns, linear, Mason-McSkimin (linear + f^4), linear + f^2 (or f^2), and linear + f^3 (or f^3). The linear spectra were found in two-thirds of the tests, followed by Mason-McSkimin relation in a quarter of the cases. In only five cases, the linear component was absent.
- (3) The transverse damping factors, η_t , converted from the linear components, ranged from 0.004 for ferrous alloys to 0.065 for FRP. Corresponding longitudinal values of η were from 0.007 to 0.048. These η and η_t for non-metals are higher than those of prototypically viscoelastic PMMA ($\eta = 0.008$ and $\eta_t = 0.013$). Even metallic values were within a factor of three, suggesting almost all engineering materials are viscoelastic.
- (4) The transverse attenuation coefficients, C_{dt} , were 1.5-times higher than the corresponding longitudinal attenuation coefficients, C_d , in 61% of the tests, while they were comparable or lower in 23 or 17%. In polymers and FRP, $C_{dt} > 2C_d$ in most cases.

- (5) Low-alloy structural steels mostly showed low C_{dt} values below 20 dB/m/MHz, which were moderately higher than C_d values. C_{dt} values for high alloy steels were higher, but most of them were below 50 dB/m/MHz. The 300-series austenitic stainless steels exhibited slightly higher attenuation than low alloy steels, but cold working reduced transverse attenuation to low levels as was the case for longitudinal attenuation.
- (6) Gray cast iron again showed frequency-squared dependence, while ductile and malleable iron had the Mason-McSkimin relation. The transverse attenuation was approximately twice than the longitudinal mode.
- (7) Aluminum alloys showed low transverse attenuation, giving C_{dt} in the range of 3 to 34 dB/m/MHz with C_{dt}/C_d ratios varying from 1.5 to 10.5. The average C_{dt}/C_d was 3.75.
- (8) A peculiar attenuation behavior of Cu and brass with the frequency-squared (and -cubed) spectra was again found in the transverse mode.
- (9) Both pure Mg and AZ61 Mg alloy showed low attenuation. In pure Mg, the transverse mode was 2.4 to 4.1 times higher, while AZ61 Mg alloy gave approximately comparable attenuation. No scattering contribution was visible.
- (10) In Ni, effects of cold work and magnetic field were stronger for the transverse mode. C_{dt} reached 300 dB/m/MHz in annealed Ni, but dropped to $\frac{1}{2}$ with strong magnets. In cold-worked Ni, both C_{dt} and C_d were 20 dB/m/MHz with no magnetic effects. High-temperature Ni alloys, Ti alloys, and tungsten were also evaluated with varied responses. Isotropic W showed comparable C_d and C_{dt} values to those of most Al alloys.
- (11) Nine engineering polymers showed about three times higher transverse attenuation than longitudinal cases. Their spectra were always linear and C_{dt} values ranged from 253 to 1830 dB/m/MHz.
- (12) Eight fiber-reinforced plastics showed higher transverse attenuation than longitudinal cases with the average C_{dt}/C_d ratio of 4.45. The previously found frequency contribution vanished, but one case of frequency-squared spectrum appeared, with all others following the linear spectra. Very high attenuation occurred in T700 CFRP and Kevlar composites. Velocity and attenuation data were converted to complex stiffness coefficients of fiber-reinforced plastics.
- (13) Twenty-four inorganic materials, 16 glasses and ceramics, six natural rocks, ADP and Si crystals, showed the linear frequency dependence except for four cases with $C_{dt} = 0$ for fused silica to 876 dB/m/MHz for granite. Marble again showed the frequency-squared spectrum, attributed to multiple scattering. ADP and Si single crystals also showed low attenuation.
- (14) Eight single crystal samples were examined. No scattering terms were found, but systematic correlations between attenuation and bonding types were not observed. Some had very low to moderate attenuation while Cu, Ni₃Al, and sapphire showed high attenuation.
- (15) Observed C_{dt}/C_d ratios were plotted against Poisson's ratios. Lower C_{dt}/C_d values were mostly between ν of 0.2 to 0.35, centering at 0.27, but this behavior seems to be unrelated to the Cauchy hypothesis.
- (16) Theories for attenuation from various scatterings provided a good basis of understanding the observed power-law behaviors. However, the main contribution to the observed attenuation, viscous damping effect, remains unresolved as only the dislocation bow-out theory [13] can give reasonable prediction to metals with low to medium strength. For high strength solids, the Gilman theory [76] may provide a new approach. Molecular dynamics and STZ approaches appear to be promising for glassy polymers.

6. Conclusions

Using verified methods of ultrasonic attenuation measurement for the transverse waves, 223 test results were obtained along with 50 additional longitudinal attenuation tests. This study and its companion work [13] experimentally surveyed the ultrasonic attenuation of various types of engineering

materials and discovered many behaviors of dynamic viscosity previously unknown. The main finding is the prevalence of the viscous damping effect in almost all the tested materials, producing the attenuation coefficients linearly dependent on frequency. The linear spectra were also modified by various scattering terms in most cases. However, the understanding of the base causes of various attenuation characteristics remains inadequate. It is hoped that systematic new inquiries in conjunction with new theoretical analyses will be conducted in the near future.

Funding: This research received no funding.

Conflicts of Interest: The author declares no conflict of interest.

Appendix A

The sound velocity data collected in this work was converted to the elastic modulus data assuming the isotropic behavior [3]. See [13] for additional information on sample materials. The values of the Young's modulus (E), shear modulus (G), and Poisson's ratio are presented below in three tables. Since the hardness values were obtained for metallic samples, these were also listed. Some of the data, such as the Young's modulus, can be found readily (although some of them may be from static measurements), but the shear modulus and Poisson's ratio are more difficult to locate (or unavailable). Note that this approach gives incorrect moduli for anisotropic materials, such as Cu and Si single crystals.

Table A1. Elastic moduli of iron and ferrous alloys.

Material	Density	v	v _t	E	G	Poisson's	Vickers
	Mg/m ³	mm/μs	mm/μs	GPa	GPa	Ratio	HN
Pure Fe cw	7.87	6.05	3.21	211.5	81.1	0.304	174
Pure Fe	7.87	6.08	3.28	219.2	84.7	0.295	91
1020	7.82	5.91	3.21	208.0	80.6	0.291	100
Low-C steel	7.82	5.93	3.26	213.3	83.1	0.283	161
4340	7.84	5.86	3.16	202.8	78.3	0.295	315
4340 (T)	7.84	5.92	3.21	208.7	80.8	0.292	315
4340 (S)	7.84	5.85	3.22	208.5	81.3	0.283	315
4142	7.84	5.92	3.23	210.7	81.8	0.288	321
4142 (T)	7.84	5.75	3.21	205.8	80.8	0.274	321
1060	7.82	5.93	3.24	211.3	82.1	0.287	198
HSLA-SM50	7.82	5.81	3.21	206.3	80.6	0.280	132
HSLA-SM50 (T)	7.82	5.86	3.23	209.2	81.6	0.282	132
HSLA-SM50 (S)	7.82	5.85	3.22	208.0	81.1	0.283	132
A533B	7.82	5.91	3.23	210.0	81.6	0.287	189
1Cr-1Mo-V	7.82	5.88	3.23	209.5	81.6	0.284	240
Tool steel T8 (T)	8.43	5.87	3.2	222.5	86.3	0.289	1155
Hardness block4	7.86	5.92	3.18	206.2	79.5	0.297	847
301	7.83	5.92	3.25	212.4	82.7	0.284	214
302	7.92	5.87	3.08	196.9	75.1	0.310	267
302	7.92	5.7	3.14	200.2	78.1	0.282	228
304	8.00	5.72	3.14	202.6	78.9	0.284	321
304	8.00	5.75	3.14	203.1	78.9	0.288	193
304 (T)	8.00	5.72	3.14	202.6	78.9	0.284	193
304 (S)	8.00	5.83	3.16	206.4	79.9	0.292	193
304L (S)	8.00	5.65	3.16	203.3	79.9	0.272	199
316	8.00	5.69	3.14	202.1	78.9	0.281	368
321	7.92	5.76	3.16	203.2	79.1	0.285	196
430 (S)	7.78	5.81	3.11	195.5	75.2	0.299	312
440A (S)	7.68	5.85	3.19	201.4	78.2	0.288	541
A286 (S)	7.94	5.75	3.16	203.5	79.3	0.284	293
17-4PH	7.81	6.1	3.17	206.4	78.5	0.315	360
17-4PH	7.65	5.84	3.17	198.5	76.9	0.291	412
Gray class 20	6.98	4.47	2.47	109.0	42.6	0.280	145
Gray class 60	7.22	5	2.79	143.2	56.2	0.274	242
Ductile 80-55-06	7.15	5.64	3.12	178.1	69.6	0.280	282
Malleabl × ferritic	7.02	5.52	3.08	169.7	66.6	0.274	145

Table A2. Elastic moduli of non-ferrous metals and alloys.

Material	Density	ν	ν_t	E	G	Poisson's	Vickers
	Mg/m ³	mm/ μ s	mm/ μ s	GPa	GPa	Ratio	HN
Al 2011	2.83	6.23	3.10	72.6	27.2	0.34	103
Al 2011	2.83	6.25	3.12	73.5	27.5	0.33	155
Al 2014	2.80	6.32	3.13	73.4	27.4	0.34	145
Al 2024	2.77	6.36	3.10	71.6	26.6	0.34	170
Al 6061	2.70	6.38	3.23	74.8	28.2	0.33	109
Al 6061	2.70	6.35	3.20	73.5	27.6	0.33	78.0
Al 7049	2.84	6.21	3.06	71.3	26.6	0.34	128
Al 7075	2.80	6.25	3.10	71.9	26.9	0.34	180
Al 7075 (T)	2.80	6.26	3.08	71.2	26.6	0.34	180
Al 7075 (S)	2.80	6.23	3.08	71.1	26.6	0.34	180
Cu single crystal	8.96	5.16	2.15	115.1	41.2	0.40	69.6
Cu electroformed	8.96	4.68	2.37	133.6	50.3	0.33	66.3
OFHC Cu	8.96	4.47	2.91	171.8	75.9	0.13	77.6
Cu 110	8.94	4.64	2.40	135.7	51.5	0.32	100
Cu 110	8.94	4.72	2.24	121.5	44.9	0.35	86.1
Cu 110	8.94	4.73	2.53	148.7	57.2	0.30	54.1
Cu 110 (S)	8.94	4.62	2.25	121.7	45.3	0.34	54.1
Brass 260	8.50	4.55	2.21	111.7	41.5	0.35	91.0
Brass 260 (T)	8.50	4.54	2.21	111.7	41.5	0.34	91.0
Brass 260 (S)	8.50	4.49	2.22	112.1	41.9	0.34	91.0
Brass 260	8.50	4.54	2.22	112.5	41.9	0.34	122
Brass 280	8.39	4.30	2.32	116.9	45.2	0.29	177
Brass 360	8.53	4.36	2.18	108.1	40.5	0.33	109
Brass 360 annealed	8.53	4.36	2.17	107.3	40.2	0.34	97.5
Cu-Zr	8.89	4.69	2.43	138.2	52.5	0.32	88.9
Cu-Al ₂ O ₃	8.90	4.54	2.42	135.7	52.1	0.30	110
Cu-Ag-Zr	9.92	4.75	2.38	149.7	56.2	0.33	110
pure Mg	1.74	5.81	3.12	43.9	16.9	0.30	40.5
Mg AZ61	1.80	5.78	2.99	42.4	16.1	0.32	91.4
Ni 200	8.91	5.72	2.97	206.8	78.6	0.32	115
Ni 200 cw	8.91	5.77	3.08	219.9	84.5	0.30	234
Monel 400	8.80	5.47	2.77	179.3	67.5	0.33	275
Inconel 600 (S)	8.50	6.35	3.76	316.8	134.6	0.23	322
Inconel 625	8.44	5.83	3.08	209.2	80.1	0.31	317
Inconel 718	8.19	5.73	3.06	199.5	76.7	0.30	152
Inconel 718 (S)	8.19	5.82	3.04	198.7	75.7	0.31	152
Inconel 738	8.11	5.72	3.08	199.4	76.9	0.30	319
Inconel 738 (T)	8.11	5.73	3.12	203.6	78.9	0.29	319
Inconel 738 (S)	8.11	5.62	3.12	201.7	78.9	0.28	319
Ni-13% Al (Ni ₃ Al)	8.10	5.53	3.29	215.0	87.7	0.23	268
Ti-6-4	4.50	6.11	3.10	114.7	43.2	0.33	330
Ti-6-6-2	4.54	6.02	3.04	111.5	42.0	0.33	359
W	19.25	5.23	2.86	405.2	157.5	0.29	299

Table A3. Elastic moduli of various materials.

Material	Density	ν_t	E	G	Poisson's
	Mg/m ³	mm/ μ s	GPa	GPa	Ratio
PMMA	0.95	1.40	4.63	1.86	0.24
PVC	1.40	1.11	4.67	1.72	0.35
PC	1.20	0.98	3.19	1.15	0.38
LDPE	0.91	1.25	3.85	1.42	0.35
HDPE	0.94	1.17	3.50	1.29	0.36
UHMWPE	0.95	1.33	4.30	1.68	0.28
Polypropylene (PP)	0.90	1.38	4.48	1.71	0.31
Nylon 6/6	1.14	1.20	4.51	1.64	0.37
Epoxy	1.39	1.38	7.05	2.65	0.33
Mortar	2.00	2.18	23.50	9.50	0.24
WC	14.51	4.07	584.4	240.4	0.22

Table A3. Cont.

Material	Density	v_t	E	G	Poisson's
	Mg/m ³	mm/ μ s	GPa	GPa	Ratio
PZT-5A	7.78	1.72	64.85	23.02	0.41
BaTiO ₃	5.70	3.60	185.6	73.87	0.26
BK7 glass	2.51	3.46	73.54	30.05	0.22
Pyrex glass	2.23	3.41	61.79	25.93	0.19
Soda-lime (S-L) glass	2.48	3.50	74.29	30.38	0.22
S-L glass, tempered	2.52	3.47	74.38	30.34	0.23
Fused silica	2.20	3.71	70.70	30.28	0.17
Clay ceramic (tile)	1.97	2.47	28.21	12.02	0.17
Porcelain	2.63	4.15	112.8	45.30	0.24
Sintered Alumina	3.42	5.47	255.1	102.3	0.25
Transparent alumina	3.90	6.19	373.1	149.4	0.25
Sapphire (R-cut)	3.98	6.78	434.4	183.0	0.19
Bonded SiC	2.32	3.42	66.87	27.14	0.23
Macor	2.52	3.10	60.06	24.22	0.24
Granite (Santa Cecilia)	2.74	2.82	56.48	21.79	0.30
Marble (Carrara)	2.83	3.34	82.15	31.57	0.30
Rock salt	2.18	2.69	38.85	15.77	0.23
Fluorite <111>	3.13	3.98	117.3	49.58	0.18
Calcite [001][110]	2.72	2.72	57.07	20.12	0.42
Calcite [001][110]	2.71	2.71	56.36	19.90	0.42
ADP <100><001>	1.80	2.20	24.87	8.71	0.43
ADP <100><010>	1.80	3.74	60.91	25.18	0.21
Quartz SX SiO ₂ X	2.56	3.28	69.06	27.54	0.25
Si SX	2.33	5.10	155.1	60.60	0.28

SX: Single crystal (fluorite, calcite, and ADP are also SX); pol: Polarization direction; <ijk> for ADP: Apparent growth orientations are used, since the Miller indices are complex.

References

- Knopoff, L. "Q". *Rev. Geophys.* **1964**, *2*, 625–660. [[CrossRef](#)]
- Mason, W.P. *Physical Acoustics and the Properties of Solids*; Van Nostrand: Princeton, NJ, USA, 1958; 402p.
- Ono, K.; Dobmann, G.; Maisl, M.; Erhard, A.; Netzelmann, U.; Wiggerhauser, H.; Helmerich, R.; Taffe, A.; Krause, M.; Kind, T.; et al. *Nondestructive Testing, Ullmann's Encyclopedia of Industrial Chemistry*; John Wiley and Sons: Hoboken, NJ, USA, 2014; Volume 24, pp. 471–584.
- Jarzynski, J.; Balizer, E.; Fedderly, J.J.; Lee, G. *Acoustic Properties—Encyclopedia of Polymer Science and Technology*; Wiley: New York, NY, USA, 2003. [[CrossRef](#)]
- ASTM D5026-15. *Standard Test Method for Plastics: Dynamic Mechanical Properties: In Tension*; ASTM International: West Conshohocken, PA, USA, 2015.
- Romanowicz, B.A.; Mitchell, B. Deep earth structure: Q of the earth from crust to core. In *Treatise on Geophysics*, 2nd ed.; Romanowicz, B., Dziewonski, A., Eds.; Elsevier: Amsterdam, The Netherlands, 2007; Volume 1, pp. 789–827. [[CrossRef](#)]
- Krautkramer, J.; Krautkramer, H. *Ultrasonic Testing of Materials*, 4th ed.; Springer: Berlin, Germany, 1990; 677p.
- Ensminger, D.; Bond, D.J. *Ultrasonics, Fundamentals, Technologies, and Applications*, 3rd ed.; Taylor & Francis Group: Boca Raton, FL, USA, 2011; 704p.
- Boller, C.; Chang, F.K.; Fujino, Y. *Encyclopedia of Structural Health Monitoring*; Wiley: Hoboken, NJ, USA, 2009; 2960p.
- Giurgiutiu, V. *Structural Health Monitoring of Aerospace Composites*; Academic Press: New York, NY, USA, 2015; 470p.
- Victrov, I.A. *Rayleigh and Lamb Waves: Physical Theory and Applications*; Plenum: New York, NY, USA, 1967; 165p.
- Ono, K. Review on structural health evaluation with acoustic emission. *Appl. Sci.* **2018**, *8*, 958. [[CrossRef](#)]

13. Ono, K. A comprehensive report on ultrasonic attenuation of engineering materials, including metals, ceramics, polymers, fiber-reinforced composites, wood, and rocks. *Appl. Sci.* **2020**, *10*, 2230. [[CrossRef](#)]
14. Winkler, K.; Nur, A. Pore fluids and seismic attenuation in rocks. *Geophys. Res. Lett.* **1979**, *6*, 1–4. [[CrossRef](#)]
15. Adam, L.; Batzle, M.; Lewallen, K.T.; van Wijk, K.J. Seismic wave attenuation in carbonates. *Geophys. Res.* **2009**, *114*, B06208. [[CrossRef](#)]
16. Mason, W.J.; McSkimin, H.J. Attenuation and scattering of high frequency sound waves in metals and glasses. *J. Acoust. Soc. Am.* **1947**, *19*, 464–473. [[CrossRef](#)]
17. Kinra, V.; Petraitis, M.; Datta, S.K. Ultrasonic wave propagation in a random particulate composite. *Int. J. Solids Struct.* **1990**, *16*, 301–312. [[CrossRef](#)]
18. Biwa, S.; Watanabe, Y.; Ohno, N. Modelling of ultrasonic attenuation in unidirectional FRP. *J. Soc. Mater. Sci. Jpn.* **2001**, *50*, 62–68. [[CrossRef](#)]
19. Rogers, P.H.; Van Buren, A.L. An exact expression for the Lommel-diffraction correction integral. *J. Acoust. Soc. Am.* **1974**, *55*, 724. [[CrossRef](#)]
20. Mielenz, K.D. Algorithms for fresnel diffraction at rectangular and circular apertures. *J. Res. Natl. Inst. Stand. Tech.* **1998**, *103*, 497–509. [[CrossRef](#)] [[PubMed](#)]
21. Kuster, G.T.; Toksöz, M.N. Velocity and attenuation of seismic waves in two-phase media. *Part I Theor. Formul. Geophys.* **1974**, *39*, 587–606.
22. Toksöz, M.N.; Johnston, D.H.; Timur, A. Attenuation of seismic waves in dry and saturated rocks: I. Laboratory measurements. *Geophysics* **1979**, *44*, 681–690. [[CrossRef](#)]
23. Wulff, A.-M.; Hashida, T.; Watanabe, K.; Takahashi, H. Attenuation behaviour of tuffaceous sandstone and granite during microfracturing. *Geophys. J. Int.* **1999**, *139*, 395–409. [[CrossRef](#)]
24. Kono, R. The dynamic bulk viscosity of polystyrene and polymethyl methacrylate. *J. Phys. Soc. Jpn.* **1960**, *15*, 718–725. [[CrossRef](#)]
25. Zimmer, J.E.; Cost, J.R. Determination of the elastic constants of a unidirectional fiber composite using ultrasonic velocity measurements. *J. Acoust. Soc. Am.* **1970**, *47*, 795–803. [[CrossRef](#)]
26. Markham, M.F. Measurement of the elastic constants of fiber composites by ultrasonics. *Composites* **1970**, *1*, 145–149. [[CrossRef](#)]
27. Hartmann, B.; Jarzynski, J. Immersion apparatus for ultrasonic measurements in polymers. *J. Acoust. Soc. Am.* **1974**, *56*, 1469. [[CrossRef](#)]
28. Pearson, L.H.; Murri, W.J. Measurement of ultrasonic wavespeeds in off-axis directions of composite materials. In *Review of Progress in Quantitative Nondestructive Evaluation*; Thompson, D.O., Chimenti, D.E., Eds.; Springer: Boston, MA, USA, 1987; Volume 6A, pp. 1093–1101.
29. Rokhlin, S.I.; Wang, W. Double through-transmission bulk wave method for ultrasonic phase velocity measurement and determination of elastic constants of composite materials. *J. Acoust. Soc. Am.* **1992**, *91*, 3303–3312. [[CrossRef](#)]
30. Wu, J. Determination of velocity and attenuation of shear waves using ultrasonic spectroscopy. *J. Acoust. Soc. Am.* **1996**, *99*, 2871–2875. [[CrossRef](#)]
31. Szabo, T.L.; Wu, J. Longitudinal and shear wave propagation in viscoelastic media. *J. Acoust. Soc. Am.* **2000**, *107*, 2437–2446. [[CrossRef](#)]
32. Castaings, M.; Hosten, B. Air-coupled measurement of plane wave, ultrasonic plate transmission for characterising anisotropic, viscoelastic materials. *Ultrasonics* **2000**, *38*, 781–786. [[CrossRef](#)]
33. Castaings, M.; Hosten, B.; Kundu, T. Inversion of ultrasonic, plan \times wave transmission data in composite plates to infer viscoelastic material properties. *NDT E Int.* **2000**, *33*, 377–392. [[CrossRef](#)]
34. Hosten, B. Ultrasonic through-transmission method for measuring the complex stiffness moduli of composite materials. In *Handbook of Elastic Properties of Solids, Liquids and Gases*; Every, A.G., Sachse, W., Eds.; Academic Press: San Diego, CA, USA, 2001; pp. 67–86.
35. Tran, H.T.K.; Manh, T.; Johansen, T.F.; Hoff, L. Temperature effects on ultrasonic phase velocity and attenuation in eccosorb and PMMA. In Proceedings of the 2016 IEEE International Ultrasonics Symposium, Tours, France, 18–21 September 2016.
36. Hartmann, B.; Jarzynski, J. Ultrasonic hysteresis absorption in polymers. *J. Appl. Phys.* **1972**, *43*, 4304. [[CrossRef](#)]

37. Simon, A.; Lefebvre, G.; Valier-Brasier, T.; Wunenburger, R. Viscoelastic shear modulus measurement of thin materials by interferometry at ultrasonic frequencies. *J. Acoust. Soc. Am.* **2019**, *146*, 3131. [[CrossRef](#)] [[PubMed](#)]
38. Saltiel, S.; Paul, A.; Selvadurai, P.A.; Brian, P.; Bonner, B.P.; Glaser, S.D.; Ajo-Franklin, J.B. Experimental development of low-frequency shear modulus and attenuation measurements in mated rock fractures: Shear mechanics due to asperity contact area changes with normal stress. *Geophysics* **2017**, *82*, M19–M36. [[CrossRef](#)]
39. Hirao, M.; Ogi, H. *EMATS for Science and Industry, Noncontacting Ultrasonic Measurements*; Kluwer: Boston, MA, USA, 2003; p. 369.
40. Ohtani, T.; Ogi, H.; Hirao, M. Electromagnetic acoustic resonance to assess creep damage in Cr-Mo-V steel, Japan. *J. Appl. Phys.* **2006**, *45*, 4526–4533. [[CrossRef](#)]
41. Rose, J.H.; Hsu, D.K. Ultrasonic reflection from rough surfaces in water. In *Review of Progress in Quantitative Nondestructive Evaluation*; Thompson, D.O., Chimenti, D.E., Eds.; Springer: Boston, MA, USA, 1987; Volume 6A, pp. 1425–1433.
42. Zhang, J.; Perez, R.J.; Lavernia, E.J. Documentation of damping capacity of metallic, ceramic and metal—Matrix composite materials. *J. Mater. Sci.* **1993**, *28*, 2395–2404. [[CrossRef](#)]
43. Hungtington, H.B. On ultrasonic scattering by polycrystals. *J. Acoust. Soc. Am.* **1950**, *22*, 362–364. [[CrossRef](#)]
44. Latiff, R.H.; Fiore, N.F. Ultrasonic attenuation in spheroidized steel. *J. Appl. Phys.* **1974**, *45*, 5182–5186. [[CrossRef](#)]
45. Coronel, V.F.; Beshers, D.N. Magnetomechanical damping in iron. *J. Appl. Phys.* **1988**, *64*, 2006–2015. [[CrossRef](#)]
46. Papadakis, E.P. Ultrasonic attenuation caused by scattering in polycrystalline metals. *J. Acoust. Soc. Am.* **1965**, *37*, 711–717. [[CrossRef](#)]
47. Stadler, F.J.; Kaschta, J.; Munstedt, H. Dynamic-mechanical behavior of polyethylenes and ethen \times /a-olefin-co-polymers. Part I. α' -Relaxation. *Polymer* **2005**, *46*, 10311–10320. [[CrossRef](#)]
48. Pethrick, R.A. Acoustical properties. In *Comprehensive Polymer Science: Supplement*; Allen, G., Aggarwal, S.L., Russo, S., Eds.; Pergamon: Oxford, UK, 1989; Volume 2, pp. 571–599.
49. Gilbert, M. Crystallinity in poly (vinyl chloride). *J. Macromol. Sci. Part C Polym. Rev.* **1994**, *34*, 77–135. [[CrossRef](#)]
50. Navarro-Pardo, F.; Martínez-Barrera, G.; Martínez-Hernández, A.L.; Castaño, V.M.; Rivera-Armenta, J.L.; Medellín-Rodríguez, F.; Velasco-Santos, C. Effects on the thermo-mechanical and crystallinity properties of nylon 6, 6 electrospun fibres reinforced with one dimensional (1D) and two dimensional (2D) carbon. *Materials* **2013**, *6*, 3494–3513. [[CrossRef](#)] [[PubMed](#)]
51. Malito, L.G.; Arevalo, S.; Kozak, A.; Spiegelberg, S.; Bellare, A.; Pruitt, L. Material properties of ultra-high molecular weight polyethylene: Comparison of tension, compression, nanomechanics and microstructure across clinical formulations. *J. Mech. Beh. Biomed. Mater.* **2018**, *83*, 9–19. [[CrossRef](#)] [[PubMed](#)]
52. Li, D.; Zhou, L.; Wang, X.; He, L.; Yang, X. Effect of crystallinity of polyethylene with different densities on breakdown strength and conductance property. *Materials* **2019**, *12*, 1746. [[CrossRef](#)]
53. Alexander, S. Amorphous solids: Their structure, lattice dynamics and elasticity. *Phys. Rep.* **1998**, *296*, 65–236. [[CrossRef](#)]
54. De Giuli, E.; Laversann-Finot, A.; Düring, G.; Lerner, E.; Wyart, M. Effects of coordination and pressure on sound attenuation, boson peak and elasticity in amorphous solids. *Soft Matter* **2014**, *10*, 5628–5644. [[CrossRef](#)]
55. De Giuli, E. Field theory for amorphous solids. *Phys. Rev. Lett.* **2018**, *121*, 118001. [[CrossRef](#)]
56. ASTM E837-13a. *Standard Test Method for Determining Residual Stresses by the Hol \times Drilling Strain-Gage Method*; ASTM International: West Conshohocken, PA, USA, 2013. [[CrossRef](#)]
57. ASTM D4093-95. *Standard Test Method for Photoelastic Measurements of Birefringence and Residual Strains in Transparent or Translucent Plastic Materials*; ASTM International: West Conshohocken, PA, USA, 2014. [[CrossRef](#)]
58. Biwa, S. Independent scattering and wave attenuation in viscoelastic composites. *Mech. Mater.* **2001**, *33*, 635–647. [[CrossRef](#)]
59. Prosser, W.H. *Ultrasonic Characterization of the Nonlinear Elastic Properties of Unidirectional Graphite/Epoxy Composites, NASA-CR-4100*; Johns Hopkins University: Baltimore, MD, USA, 1987; 198p.

60. Roman, I.; Ono, K. *AE Characterization of Failure Mechanisms in Woven Roving Glass-fiber Epoxy Composites, Progress in Acoustic Emission II*; Japanese Society for Non-Destructive Inspection: Tokyo, Japan, 1984; pp. 496–503.
61. Liu, W.; Zhang, L. Mechanisms of the complex thermo-mechanical behavior of polymer glass across a wide range of temperature variations. *Polymers* **2018**, *10*, 1153. [[CrossRef](#)] [[PubMed](#)]
62. Sane, S.B.; Cagin, T.; Goddard, W.A.; Knauss, W.G. Molecular dynamics simulations to compute the bulk response of amorphous PMMA. *J. Comput. Aided Mater. Des.* **2001**, *8*, 87–106. [[CrossRef](#)]
63. Hernandez, C.A.S. Molecular Dynamic Simulation of Thermo-Mechanical Properties of Ultra-Thin Poly (Methyl Methacrylate) Films. Ph.D. Thesis, Texas A&M University, College Station, TX, USA, 2010; 155p.
64. Fang, Q.; Tian, Y.; Wu, H.; Li, J. Revealing the deformation mechanism of amorphous polyethylene subjected to cycle loading via molecular dynamics simulations. *RSC Adv.* **2018**, *8*, 32377–32386. [[CrossRef](#)]
65. Barrat, J.-L.; Baschnagel, J.; Lyulin, A. Molecular dynamics simulations of glassy polymers. *Soft Matter* **2010**, *6*, 3430–3446. [[CrossRef](#)]
66. Bouchbinder, E.; Langer, J.S.; Procaccia, I. Athermal shear-transformation-zone theory of amorphous plastic deformation, I. basic principles. *Phys. Rev. E* **2007**, *75*, 036107. [[CrossRef](#)]
67. Bouchbinder, E.; Langer, J.S.; Procaccia, I. Athermal shear-transformation-zone theory of amorphous plastic deformation, II. Analysis of simulated amorphous silicon. *Phys. Rev. E.* **2007**, *75*, 036108. [[CrossRef](#)]
68. Demkowicz, M.J.; Argon, A.S. Liquidlike atomic environments act as plasticity carriers in amorphous silicon. *Phys. Rev. B* **2005**, *72*, 245205. [[CrossRef](#)]
69. Fitzgerald, J.V.; Laing, K.M.; Bachman, G.S. Temperature variation of the elastic moduli of glass. *Trans. Soc. Glass Tech.* **1952**, *36*, 90–104.
70. Chen, B.; Li, S.; Zong, H.; Ding, X.; Sun, J.; Ma, E. Unusual activated processes controlling dislocation motion in body-centered-cubic high-entropy alloys. *Proc. Natl. Acad. Sci. USA* **2020**, *117*, 201919136. [[CrossRef](#)]
71. Greaves, G.N.; Greer, A.L.; Lakes, R.S.; Rouxel, T. Poisson's ratio and modern materials. *Nat. Mater.* **2011**, *10*, 823–837. [[CrossRef](#)]
72. Greaves, G.N. Poisson's ratio over two centuries: Challenging hypotheses. *Notes Rec. R. Soc.* **2013**, *67*, 37–58. [[CrossRef](#)] [[PubMed](#)]
73. Bhatia, A.B. *Ultrasonic Absorption, An Introduction to the Theory of Sound Absorption and Dispersion in Gases, Liquids and Solids*; Clarendon Press: Oxford, UK, USA, 1967; 427p.
74. Nowick, A.S.; Berry, B.S. *Anelastic Relaxation in Crystalline Solids*; Academic Press: New York, NY, USA, 1972; 694p.
75. Blanter, M.S.; Golovin, I.S.; Neuhäuser, H.; Sinning, I.R. *Internal Friction in Metallic Materials. A Handbook*; Springer: Berlin, Germany, 2007; 542p.
76. Gilman, J.J. Chemical theory of dislocation mobility. *Mater. Sci. Eng.* **2005**, *409*, 7–12. [[CrossRef](#)]

